Ocean Modelling 184 (2023) 102228

Contents lists available at ScienceDirect

Ocean Modelling

journal homepage: www.elsevier.com/locate/ocemod

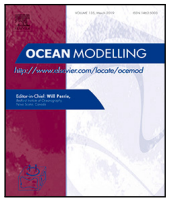

Arctic ice-ocean interactions in an 8-to-2 kilometer resolution global model

Elizabeth C. Fine [a,b,*], Julie L. McClean [a], Detelina P. Ivanova [c], Anthony P. Craig [a], Alan J. Wallcraft [d], Eric P. Chassignet [d], Elizabeth C. Hunke [e]

[a] Scripps Institution of Oceanography, University of California, San Diego, 9500 Gilman Drive, 0230, La Jolla, 92093-0230, CA, USA
[b] Woods Hole Oceanographic Institution, 86 Water St, Falmouth, 02543, MA, USA
[c] Climformatics, Inc, Freemont, 94555, CA, USA
[d] Center for Ocean-Atmospheric Prediction Studies, Florida State University, Tallahassee, 32306, FL, USA
[e] Los Alamos National Laboratory, 87545, New Mexico, USA

ARTICLE INFO

Dataset link: https://doi.org/10.6075/J0XK8FQH

Keywords:
Arctic ocean
Modeling
Sea ice
Upper ocean
Heat content
Halocline

ABSTRACT

In the last decades, the Arctic climate has changed dramatically, with the loss of multiyear sea ice one of the clearest consequences. These changes have occurred on relatively rapid timescales, and both accurate short-term Arctic prediction (e.g., 10 days to three months) and climate projection of future Arctic scenarios present ongoing challenges. Here we describe a representation of the Arctic ocean and sea ice in a ultrahigh resolution simulation in which the horizontal grid mesh reduces from 8 km at the equator to 2 km at the poles (UH8to2) for the years 2017–2020. We find the simulation reproduces observed distributions of seasonal sea-ice thickness and concentration realistically, although concentration is biased low in the spring and summer and low biases in thickness are found in the central and eastern basins in the fall. Volume, fresh water, and heat transports through key passages are realistic, lying within observationally determined ranges. Climatological comparisons reveal that the UH8to2 Atlantic Water is shallower, warmer, and saltier than the World Ocean Atlas 2018 climatology for 2005–2017 in the eastern basin. Our analysis suggests that these biases, combined with a lack of stratification in the upper 100 m of the simulated ocean, contribute to the winter biases in modeled sea ice thickness. This relationship between biases in the sea ice and ocean points to a potential positive feedback within the model, illuminating challenges for long term model predictive power in a changing Arctic climate.

1. Introduction

Arctic sea ice decline is one of the clearest effects of global warming, characterized by a loss of both sea ice area and volume (Stroeve et al., 2012; Cohen et al., 2014; Perovich and Richter-Menge, 2015; Lindsay and Schweiger, 2015). Concurrently, the Arctic Ocean is also responding to a changing climate. The reduction of sea ice cover has enhanced air–sea exchanges of momentum, freshwater, and heat, as well as altered the albedo of the surface Arctic, leading to increased warming due to solar radiation. The subsurface Arctic Ocean waters are fed by inflowing waters from the Atlantic and Pacific Oceans, which have also warmed in recent years (Woodgate et al., 2012; Carmack et al., 2015; Timmermans et al., 2018). Additional changes in fresh water and atmospheric circulation have led to increased freshwater storage in the western Arctic (Proshutinsky et al., 2019). These changes in ocean circulation have resulted in a warmer and saltier eastern Arctic (Polyakov et al., 2017) and a more stratified western Arctic with shallower winter mixed layers (Peralta-Ferriz and Woodgate, 2015).

Arctic sea ice is associated with a very fresh mixed layer, which lies above a strong halocline. This halocline stratification is maintained by surface freshwater fluxes from net precipitation and river runoff, as well as relatively low turbulent mixing rates over much of the basin, preserving a strong vertical gradient. Sea ice itself has been hypothesized to contribute to the maintenance of this strong gradient, as sea ice melt contributes to a fresh ice-associated surface layer (Toole et al., 2010).

Beneath this fresh mixed layer lie saltier water masses originating in the Atlantic and Pacific Oceans (Rudels et al., 2004; Timmermans et al., 2014). Atlantic Water enters the Arctic via Fram Strait and the Barents Sea Opening. This inflowing water subducts beneath the fresh surface layer to form the Atlantic Water mass, separated from the surface mixed layer by a halocline (Rudels et al., 2004). Pacific water enters the Arctic through Bering Strait, and is modified in the shallow Chukchi Sea (Pickart et al., 2005; Woodgate et al., 2012; Corlett and Pickart, 2017). This inflowing water is relatively warm and fresh in the summer, and cold and saltier in the winter, so that it forms two distinct, seasonally-ventilated water masses: the Pacific Summer Water and Pacific Winter Water (Timmermans et al., 2014; Pickart et al., 2005). These water masses are found above the saltier Atlantic Water throughout the western Arctic.

* Corresponding author at: Scripps Institution of Oceanography, University of California, San Diego, 9500 Gilman Drive, 0230, La Jolla, 92093-0230, CA, USA.
E-mail address: ecfine@ucsd.edu (E.C. Fine).

https://doi.org/10.1016/j.ocemod.2023.102228
Received 30 August 2022; Received in revised form 12 April 2023; Accepted 18 May 2023
Available online 27 May 2023

Model representations of these water masses vary in accuracy. Intercomparisons of 15 global ocean–sea ice models show a large range of variability in modeled temperature and freshwater content in the interior Arctic (Wang et al., 2016b; Ilicak et al., 2016). Individual model representations of the temperature at 400 m depth (approximately corresponding to the depth of Atlantic Water) had differences of up to 4 °C. Higher resolution global and regional models often have similar biases; using a regional model with 10 km horizontal resolution, Hordoir et al. (2022) found a cool bias of about 1 °C in the temperature of Atlantic Water, while using a global model with 4.5 km resolution Wang et al. (2018) found a warm and shallow bias in Atlantic Water.

Reproducing the strong halocline in the western Arctic is also a challenge for coupled atmosphere–ice–ocean models, global ice-ocean models, and regional Arctic models. Rosenblum et al. (2021) found Community Earth System Models 1 and 2 (CESM1 and CESM2) have a saltier surface salinity in the western Arctic than observed in the years 2006–2012, consistent with other studies showing reduced western Arctic upper-ocean stratification in global models (Wang et al., 2016b; Holloway and Proshutinsky, 2007). Even in high-resolution models upper-ocean stratification is frequently biased low. Jin et al. (2018) and Hordoir et al. (2022) both found insufficient stratification in the upper ocean of the western Arctic in 9–10 km regional models. Jin et al. (2018) found that incorporating a parameterization for brine rejection (Jin et al., 2012; Nguyen et al., 2009) improved the upper-ocean salinity structure. Global models often apply a restoring of sea-surface salinity at high latitudes to address this drift; in some cases this correction is sufficient to improve the upper-ocean stratification (Wang et al., 2018; Uotila et al., 2019).

The Pacific Summer Water temperature maximum is occasionally assessed as part of model validation; where upper-ocean temperatures in the western Arctic are presented, this maximum is frequently absent in both one degree (Ilicak et al., 2016; Lavoie et al., 2022) and eddy-permitting (Wang et al., 2018) models. Models generally vary in their representation of the dynamics that bring Pacific-origin water into the Arctic basins. Aksenov et al. (2016) find large variability in both the fraction and distribution of Pacific-origin water in six Arctic models, while in a regional model specialized to study western Arctic boundary currents, Leng et al. (2021) note that even 4.5 km model resolution under-resolves important pathways for Pacific inflows, possibly leading to biases in the simulated off-shelf transport. However, Zhang et al. (2016) describe a regional model which successfully reproduces both the Pacific Summer Water temperature maximum and associated halocline stratification. This model assimilates both sea ice concentration and sea surface temperature, and uses a 5 m vertical grid in the upper 80 m of the ocean, with horizontal resolution of 16–20 km in the Beaufort Gyre region. The model grid is optimized to resolve the Chukchi, Beaufort, and Bering Seas, with 26 grid cells spanning the Bering Strait (Zhang et al., 2016).

Misrepresentations of the Atlantic and Pacific water masses may have significant implications for model predictive capacity on seasonal, interannual, and decadal timescales. Ice-ocean heat fluxes play an important role in regulating the Arctic sea ice growth/melt cycle, with approximately half of the net heat flux to sea ice coming from the ocean (Carmack et al., 2015). Positive feedback cycles have been hypothesized to potentially contribute to current and future Arctic climate change. These include a positive feedback between the wind, ice, and ocean, in which

1. Sea ice decline leads to increased momentum transfer into the upper ocean;
2. Increased upper-ocean shear leads to increased ocean mixing;
3. Increased ocean mixing results in the entrainment of more subsurface oceanic heat into the mixed layer, and
4. Increased mixed layer heat results in increased sea ice decline.

Recent observations suggest that this feedback may be leading to accelerated sea ice decline in the eastern Arctic (Polyakov et al., 2020a,b). A second hypothesized feedback loop is related to the effect of brine rejection during sea ice formation, as follows:

1. Sea ice decline leads to increasingly large regions of summertime open water;
2. In autumn, freeze-up occurs over an increased ocean area, resulting in overall increased brine rejection;
3. Brine rejection leads to convection, deepening the ocean mixed layer;
4. Subsurface oceanic heat is entrained into the ocean mixed layer, melting more ice (perhaps at a spatial shift due to horizontal advection of the ice and ocean).

These two feedback loops both suggest that sea ice decline may be associated with deepening ocean mixed layers and increased entrainment of heat from subsurface water masses. These positive feedbacks are inherently unstable, so that small initial discrepancies in sea ice representation or upper-ocean heat content may have large downstream impacts. Thus, accurate model representation of the stratification and heat content of the upper Arctic ocean is important, both to accurately capture the current state of the ice-ocean system and to inform future projections.

In the current work, we use output from a new atmospheric reanalysis-forced ultrahigh resolution global ocean–sea ice model to investigate the potential influence of the upper Arctic ocean on Arctic sea ice. The model's horizontal resolution varies from 8 km at the equator to 2 km at the poles. As the Rossby radius in the Arctic Ocean is generally less than 10 km and as low as 1 km in the shelf seas, this model configuration allows for the resolution of mesoscale processes which are not simulated in even 0.25° models (Nurser and Bacon, 2014). We consider the model output along with synoptic observational data from autonomous profiling drifters. Combining these approaches allows us to leverage the model's capacity to resolve mesoscale processes along with concurrent year-round observations from an environment that is logistically difficult to sample due to sea ice, extreme weather conditions, and its distance from deep water ports. These approaches are complementary, as while the autonomous profilers provide high along-track resolution as they drift within the Arctic Ocean, the data is limited to the profiler pathways. Observational data is particularly limited in the Eurasian Basin, where the signal of warming Atlantic water is strongest and this water mass is closest to the surface. Conversely, the ultrahigh resolution model provides a complete picture of the modeled ocean circulation; however, like many other Arctic simulations (Ilicak et al., 2016; Wang et al., 2016b, 2018; Jin et al., 2018; Hordoir et al., 2022) it contains biases, including overly warm Atlantic Water and overly weak near-surface stratification. Thus, our goals are two-fold: first, to understand biases in the representation of upper-ocean stratification and heat content in the Arctic region of this ultrahigh resolution global model, and secondly, to examine the impact of these biases on ice-ocean heat fluxes.

While our results are inherently linked to characteristics of this particular model, accurately modeling the temperature, salinity, and dynamics of the upper Arctic Ocean is an ongoing challenge. Thus the relationships we find between these biases and ice-ocean interaction can be used to inform future modeling efforts and observational design by setting priorities for bias reduction, optimization of grid choices, and highlighting where new observations are most necessary. A key finding of this work is that enhanced horizontal resolution is not on its own sufficient to avoid significant biases in ice-ocean heat fluxes. Resolving or effectively parameterizing the mixed layer processes that mediate availability of oceanic heat to sea ice is necessary to avoid biases that will tend to result in increasing model drift due to the positive feedbacks discussed above.

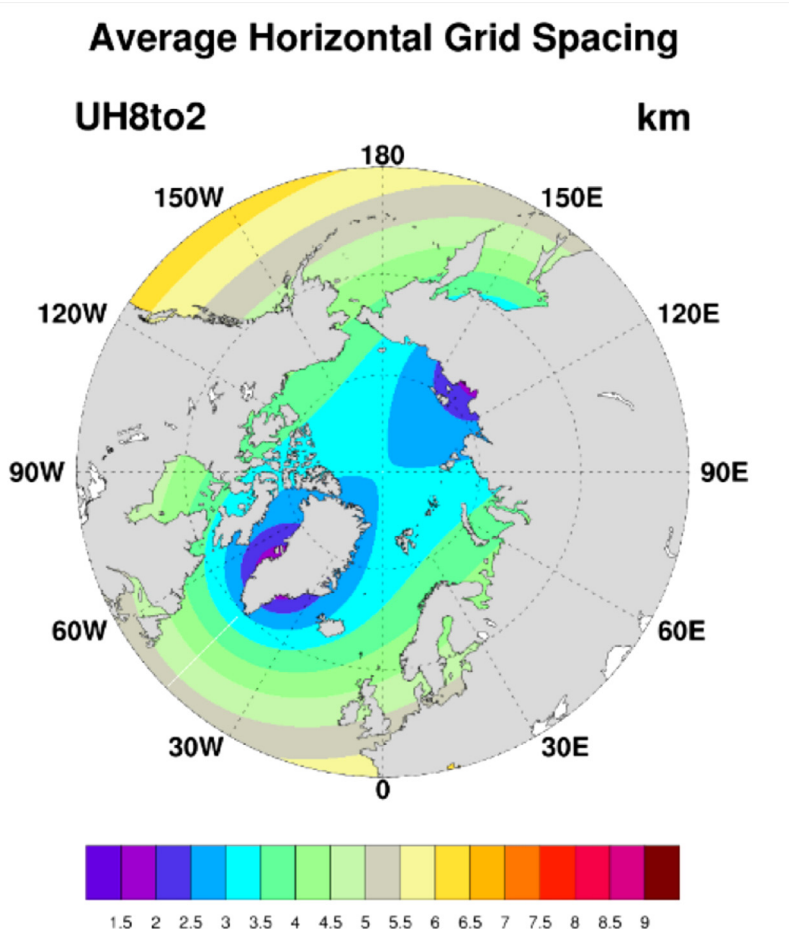

Fig. 1. Square root of horizontal area (km) of grid cells in the Arctic region of the UH8to2 POP model.

The following sections are organized as follows. In Section 2 we discuss methods, including the model set-up, climatologies, and observational datasets, as well as the calculation of all quantities considered in the following analysis. In Section 3 we discuss the model realism relative to both climatology and various observational datasets, focusing on the model representation of Arctic gateway fluxes, circulation, sea ice, and hydrography. In Section 4 we discuss the potential impacts of model biases on ice-ocean heat fluxes. In Sections 5 and 6 we conclude with a summary of results and discussion of their implications.

2. Methods

2.1. UH8to2 model

The coupled ocean/sea-ice simulation used in this study is configured on a new tripolar global grid with north poles located in Greenland and Siberia. The horizontal grid decreases from 8 km at the equator to 2 km at the poles and resolves mesoscale processes more fully at high latitudes (poleward of 50°N and 50°S) than standard 0.1° global grids (e.g., Maltrud and McClean 2005, McClean et al. 2011). Hence, we designate this mesh as the "ultrahigh 8to2" (UH8to2). The ocean and sea-ice component models used in the UH8to2 simulation are the Parallel Ocean Program2 (POP2; Dukowicz and Smith 1994) and CICE5 (Hunke et al., 2015), respectively. The simulation ran from July 2016 through December 2020 and was forced with Japanese 55-year Atmospheric Reanalysis-driving ocean (JRA55-do; Tsujino et al. 2018) surface fluxes over this period.

The UH8to2 simulation was produced using the Department of Energy (DOE)'s Energy Exascale Earth System Model "HiLAT" code (E3SMv0-HiLAT, referred to hereafter as HiLAT, Hecht et al. 2019); HiLAT was derived from the CESM1 (Hurrell et al., 2013). HiLAT uses the Regional Arctic System Model (RASM) coupling scheme (Roberts et al., 2015); modifications were made to Coupler 7 (CPL7; Craig et al. 2012) to allow for high-frequency inertial sea-ice oscillations. In this simulation the ocean, sea-ice, and the reanalysis atmosphere are coupled every 20 min.

Over the Arctic Ocean, the UH8to2 horizontal grid has a resolution of 2–4 km (Fig. 1). The positioning of the two north poles produces the highest horizontal resolution in the shelf-seas adjacent to Siberia and Greenland and horizontal resolution of less than 3.5 km in the central Arctic. The model has 60 z-levels. The vertical spacing varies from 10 m over the upper 160 m of the ocean to 250 m at depth; the maximum model depth is 5500 m. Given that Arctic mixed layers can be less than 10 m in depth, this vertical grid spacing is insufficient to fully resolve mixed layer processes, as discussed in the sections that follow. Partial bottom cells are used to enhance the smoothness of the bottom topography. The model bathymetry is based on the General Bathymetric Chart of the Oceans 30 arc second grid (GEBCO_2014, Weatherall et al. 2015).

JRA55-do forcing was constructed from atmospheric surface fields obtained from JRA-55 that consists of an atmospheric model and a data-assimilation scheme. Adjustments were made to the JRA-55 surface forecast fields, both in the Arctic and elsewhere, to better agree with independent *in situ* observations. JRA55-do comprises these corrected surface forecast fields, has a horizontal resolution of about 55 km (0.25°), and is available on a three-hourly basis from 1958 through 2020 (Tsujino et al., 2018). It includes daily river runoff, as well as representations of ice sheet and ice-shelf discharge and melting around Greenland (Bamber et al., 2018) and Antarctica (Depoorter et al., 2013). Independent Arctic atmospheric measurements are scarce, and it is beyond the scope of this study to validate the JRA55-do; however

we note that biases in JRA55-do, particularly in downward long wave radiation flux, may result in biases in the UH8to2 upper-ocean and ice fields. As is standard practice for forced ocean models (Yeager et al., 2012), weak (relaxation time scale of four years) sea surface salinity restoring to Polar Science Center Hydrographic Climatology 3.0 (Steele et al., 2001) is added to the surface freshwater fluxes to limit drift in the ocean. This climatology was last updated in 2005, so this restoring may introduce a small positive salinity bias relative to current Arctic conditions (Tsujino et al., 2018). However, intermodel comparisons suggest that models are not especially sensitive to the strength of sea surface salinity restoring, with subgridscale parameterizations and grid resolutions explaining more intermodel variability than variation in the strength of the sea surface salinity restoring (Danabasoglu et al., 2014). In light of this analysis we do not expect the restoring to have a significant impact on our results on seasonal or interannual timescales relative to factors such as vertical grid size and atmospheric forcing.

In the UH8to2 simulations, CICE5 uses an elastic-anisotropic-plastic (EAP) sea-ice rheology (Tsamados et al., 2013) to compute sea-ice velocities and mushy-layer thermodynamics (Turner et al., 2013) to obtain ice growth and melt rates. The "level-ice" scheme (Hunke et al., 2013) produces melt ponds that pool on sea ice that is not deformed. Thermal conductivity of sea ice is represented using the "bubbly" brine model (Pringle et al., 2007), while the transfer of solar radiation between snow and sea ice is modeled using the Delta-Eddington multiple scattering parameterization (Briegleb and Light, 2007). Five sea-ice thickness categories are employed and the sea-ice strength parameterization is based on Rothrock (1975), which closely relates ice strength to the ridging scheme.

Initial conditions (ICs) for the UH8to2 simulation were chosen to best represent near-present conditions (late 2010s onwards) by using an ocean/sea-ice state from a data assimilative ocean and sea-ice modeling system that provides realistic forecasts for the study region and period. The system is the Global Ocean Forecasting System 3.5 (GOFS 3.5, Metzger et al. 2020); it uses 1/25° HYCOM (Bleck, 2002; Chassignet et al., 2003) and CICE5, and is branched from a multi-decadal spin-up based on earlier forward and data assimilative HYCOM/CICE4 simulations (Chassignet et al., 2009; Metzger et al., 2014). GOFS3.5 produced forecasts from January 2017 onwards and showed markedly improved depictions of Arctic sea-ice relative to GOFS3.1 that used CICE4 (Metzger et al., 2020). This initialization approach was used instead of carrying out a multi-decadal model spin-up initialized from a temperature and salinity climatology that was constructed using observations from earlier decades. A multi-decadal spin-up was precluded by the length of real-world time and computational cost required to run the UH8to2 for multiple decades leading up to 2016 with no guarantee that model drift would not degrade the resulting simulation for the study period.

The ocean component of UH8to2 was initialized from rest using smoothed instantaneous full-depth potential temperature and salinity fields that were interpolated onto the UH8to2 grid from the 07/01/2017 GOFS 3.5 ocean state. We chose boreal summer for the start of the run so that the model spun-up through the seasonal sea-ice minimum in September and fall freeze-up, allowing CICE5 to maximize its sea-ice coverage under the JRA55-do forcing. When we started the simulation, JRA55-do forcing was only available through 2019 (2020 forcing became available later in the project). Hence, to lengthen the simulation, we started it using forcing from one year earlier in summer (07/01/2016). Although this choice resulted in a mismatch between the date of the forcing and the ICs, it was considered a better option than using concurrent ICs from GOFS3.1 that produced less realistic sea-ice than GOFS3.5.

To maintain consistency with the GOFS3.5 ocean ICs (e.g., the match between sea-ice coverage and surface temperature and salinity to avoid unrealistic ocean/sea-ice instabilities), the use of sea-ice thickness and concentration from GOFS3.5 on 07/01/2017 was considered to be optimal in the UH8to2 sea-ice ICs. Moreover, satellite-derived sea-ice concentration is assimilated into the GOFS3.5 sea-ice model (Metzger et al., 2020). However, interpolating the full GOFS3.5 CICE5 instantaneous restart onto the UH8to2 grid would very likely have produced unphysical effects. Instead, we used an instantaneous CICE5 restart from a separate UH8to2 simulation (Morrison, 2022) as a background state and replaced and merged, respectively, its thickness and concentration fields, with those from GOF3.5. The background sea-ice concentration field was replaced by the GOFS3.5 concentration for all grid cells in which the difference between the two fields was greater than 1%. Other sea-ice variables adjusted to these inserted fields during the spin-up phase. The simulation from which the background state was taken was forced with interannually-varying Coordinated Ocean–Ice Reference Experiment II air–sea fluxes (Large and Yeager, 2009) and was run for an earlier period (1975 to the mid-1990s at the time). The month and day of the background state, 07/01/1994, were chosen to match those of the start date of the 2016–2020 simulation used in this study; visual inspection of the 07/01/1994 sea-concentration and thickness found them to be realistic. The UH8to2 grid and interpolation files used by the coupler to exchange fluxes between the component grids are common to both UH8to2 simulations and were developed and tested as part of the set-up of the CORE-forced UH8to2 simulation.

A 10-day adjustment phase followed the initialization. First, model sea-ice and ocean velocities were allowed to develop over two days while the potential temperature and salinity fields were restored to the GOFS ocean fields with a tight four-hour timescale. The model then ran freely for seven days, followed by a day over which the tight (four hour) restoring of ocean potential temperature and salinity was used again to allow further adjustment of model sea-ice and ocean velocities. The simulation was then run forward from 07/11/2016 through 12/31/2020. We treat the period from July–December 2016 as the spin up phase as a rapid decrease in global mean kinetic energy occurred during this period (not shown); this decline leveled off in early 2017. Hence, we analyze the period from January 2017–December 2020 in this study.

Daily-averaged ocean state variables, surface fluxes, horizontal heat flux covariance terms and standard sea-ice variables (e.g., thickness, concentration, drift, thermodynamic and dynamic terms) were archived for the entire period of the simulation.

2.2. Satellite-derived sea-ice data

Simulated monthly-averaged sea ice extent and concentration are compared to a dataset compiled from three satellite instruments: the Nimbus-7 Scanning Multichannel Microwave Radiometer (SSMR), the Defense Meteorological Satellite Program's Special Sensor Microwave/Imager (SSM/I), and the Special Sensor Microwave Imager/Sounder (SSMIS, Comiso 2017). Satellite sea ice extent is processed using both bootstrap and NASA Team algorithms (Stroeve and Notz, 2018). Simulated monthly sea ice thickness was compared to observations from CryoSat −2 (Laxon et al., 2013; Kurtz and Harbeck, 2017). Monthly-averaged values of observed sea ice extent, concentration, and thickness were used for these comparisons. Thickness observations are only available from October through April, due to satellite measurement problems caused by melt ponds during the Arctic summer months (Kurtz and Harbeck, 2017).

2.3. Ocean climatology

The scarcity of data collected in the Arctic Ocean makes model validation a challenge. In our analysis we compare the model with the 1/4° World Ocean Atlas 2018 (Boyer et al., 2018). This climatology incorporates Arctic data from the National Centers for Environmental Information archives. We used the version that depends only on data collected in the most recent years (2005–2017) so that the climatology represents the modern Arctic as much as possible. Throughout the rest of the text, this climatology is referred to as "WOA18". There are some discrepancies between this climatology and observational data from the

Table 1
ITP deployments that overlapped with the 2017–2020 model run. Dates are given of the first and last overlapping profiles. The total number of profiles refers to the number which overlapped with the model run.

ITP #	First profile	Last profile	Region	Data Status	# profiles
93	1-Jan-2017	3-Jan-2017	Eastern Arctic	Level 2	7
94	8-Oct-2019	19-Aug-2020	Eastern Arctic	Level 3	481
95	12-Apr-2017	6-Jan-2018	Eastern Arctic	Level 3	1075
97	1-Jan-2017	5-Oct-2017	Beaufort Sea	Level 3	554
99	1-Jan-2017	21-Jan-2017	Beaufort Sea	Level 3	40
100	19-Sep-2017	15-Dec-2017	Beaufort Sea	Level 3	174
101	17-Sep-2017	26-Mar-2018	Beaufort Sea	Level 3	380
102	11-Oct-2019	26-Mar-2018	Eastern Arctic	Level 3	2142
103	3-Oct-2018	12-Oct-2019	Beaufort Sea	Level 3	6621
104	6-Oct-2018	29-Aug-2019	Beaufort Sea	Level 3	6223
105	8-Oct-2018	29-Aug-2019	Beaufort Sea	Level 3	6062
107	19-Sep-2018	23-Sept-2019	Beaufort Sea	Level 3	738
108	18-Sep-2017	8-Sept-2018	Beaufort Sea	Level 3	1000
109	22-Sep-2018	15-Dec-2018	Beaufort Sea	Level 3	167
110	21-Sep-2018	7-Aug-2019	Beaufort Sea	Level 2	638
111	7-Oct-2019	5-Aug-2020	Eastern Arctic	Level 3	604
112	24-Sep-2019	12-Nov-2019	Beaufort Sea	Level 3	95
113	20-Sep-2019	30-Dec-2020	Beaufort Sea	Level 2	5347
114	22-Sep-2019	30-Sept-2020	Beaufort Sea	Level 2	4404
116	22-Aug-2019	2-Jan-2020	Central Arctic	Level 2	528
117	21-Sep-2019	2-Jan-2020	Beaufort Sea	Level 2	204
118	22-Sep-2019	2-Jan-2020	Beaufort Sea	Level 2	202
119	20-Sep-2019	1-Jan-2020	Beaufort Sea	Level 3	205
120	23-Sep-2020	30-Dec-2020	Beaufort Sea	Level 2	391
121	21-Sep-2020	30-Dec-2020	Beaufort Sea	Level 2	199

2017–2020 period over which the model was run; see Fig. 3 and the next section for details.

Velocity observations are especially sparse in the Arctic, and climatologies do not generally include representations of ocean velocity. Thus we compare model velocities to the Arctic Subpolar gyre sTate Estimate (ASTE; Nguyen et al. 2021). The Arctic Subpolar gyre sTate Estimate is a dynamically-constrained ocean–sea ice model-data synthesis with nominal 0.3° resolution, and spans the time period 2002–2017. 2017 is the only year over which both ASTE and the UH8to2 simulations are available, thus we limit the velocity comparison to this year.

2.4. Ice-Tethered Profilers

Ice-Tethered Profilers (ITPs; Krishfield et al. 2008, Toole et al. 2010) are autonomous drifters embedded in Arctic sea ice that measure temperature and salinity to 750 m depth. The instrument consists of a surface buoy which lies above the sea ice, a wire which is suspended from the surface buoy to the profiling depth, and a wire-crawling profiler that traverses the suspended wire. The end of the wire carries a weight to ensure the wire stays taut. Most ITPs initiate two profiles per day, during which the profiler crawls along the wire at ~0.25 m/s, so that each profile is completed in about an hour, although a subset of the ITPs that were deployed for specific experiments initiate profiles more frequently. Twenty-five ITPs were deployed during the four-year model run, primarily in the western Arctic (Table 1). Where Level 3 (gridded to two decibars in the vertical and quality controlled) data were available, we used them, while for missions in which only Level 2 processing was completed we interpolated data to the same two decibar pressure grid and removed profiles with clearly unphysical temperature or salinity values. Model ITP deployments and matched profiles were constructed by sampling the daily model output at the nearest model grid point to the starting location of each ITP profile on the day the profile began. A total of 38927 matched profiles were obtained in this manner.

2.5. Calculated quantities

2.5.1. Hydrographic characteristics

The Atlantic Water and Pacific Summer Water are the two primary reservoirs of subsurface heat in the Arctic Ocean. Characteristics of these water masses are defined as follows. “Atlantic Water depth” was defined as the depth of the shallowest 0 °C isotherm deeper than a threshold depth, with salinity greater than 34.8 (Rudels et al., 2004). In most of the Arctic Ocean we use 50 m depth as this threshold. In the western Arctic, warm Pacific Summer Water is found at depths between 40–100 m (Timmermans et al. 2014, see below), so we apply a deeper threshold of 125 m in observational data (UH8to2 Pacific Summer Water is cooler so these two choices produce identical results for the UH8to2 Atlantic Water). “Atlantic Water temperature” is defined as the maximum temperature between this depth and the deeper 0 °C isotherm occurring beneath it. Pacific Summer Water is defined following Timmermans et al. (2014) as the subsurface temperature maximum in the western Arctic between 40–100 m depth.

The mixed layer depth (MLD) is identified from density profiles following Peralta-Ferriz and Woodgate (2015), who used a density cutoff $\delta\sigma$ referenced to the surface density to define the mixed layer depth. In the model we treat the density in the uppermost ocean bin (spanning 0–10 m depth) as the “surface” density, and in ITP data we use the shallowest CTD measurement, provided it is shallower than 10 m depth, following Cole and Stadler (2019). Different Arctic mixed layer studies use different thresholds for the density cutoff, including 0.03 kg m^{-3}, 0.1 kg m^{-3}, and 0.25 kg m^{-3} (Toole et al., 2010; Peralta-Ferriz and Woodgate, 2015; Cole and Stadler, 2019). In the UH8to2 model, we found that none of these thresholds produced a mixed layer depth that followed the deepening of the layer of high stratification seen during the winter (Fig. 2). However, using a more generous threshold of 0.5 kg m^{-3} for both the UH8to2 density and observed data resulted in a mixed layer depth that tracked the maximum stratification. This choice led to only slight differences in mixed layer depths in observations relative to using 0.25 kg m^{-3}, and did not impact our qualitative conclusions (Fig. 2). We additionally considered a mixed layer definition based on the depth of the sharpest change in stratification (e.g., Jackson et al. 2010), but prefer the threshold approach for this application as in cases where there is both a remnant winter mixed layer and a developing spring mixed layer, the threshold approach tends to select for the shallower mixed layer, which is more relevant for our investigation of ice-ocean interactions.

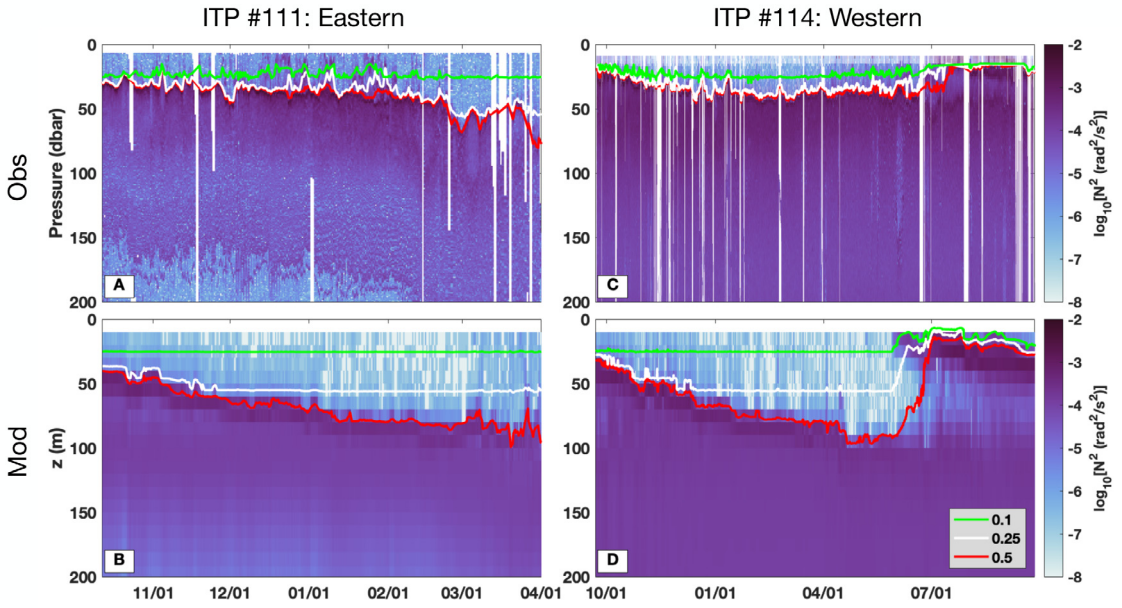

Fig. 2. Stratification (N^2, units of rad^2 s^{-2}) and mixed layer depths over two example ITP deployments as follows: (a) ITP 111 (eastern Arctic), observed; (b) ITP 111 (eastern Arctic), modeled; (c) ITP 114 (western Arctic), observed; and (d) ITP 114 (western Arctic), modeled. The three lines represent mixed layer depths calculated using a threshold difference in $\delta\sigma$ of 0.1 (green), 0.25 (white), and 0.5 (red) kg m^{-3}. Throughout the rest of the study, $\delta\sigma$ = 0.5 kg m^{-3} is used to define the mixed layer depth, as this value agreed best with the evolution of the deepening peak in N^2 through the winter, especially in the model fields.

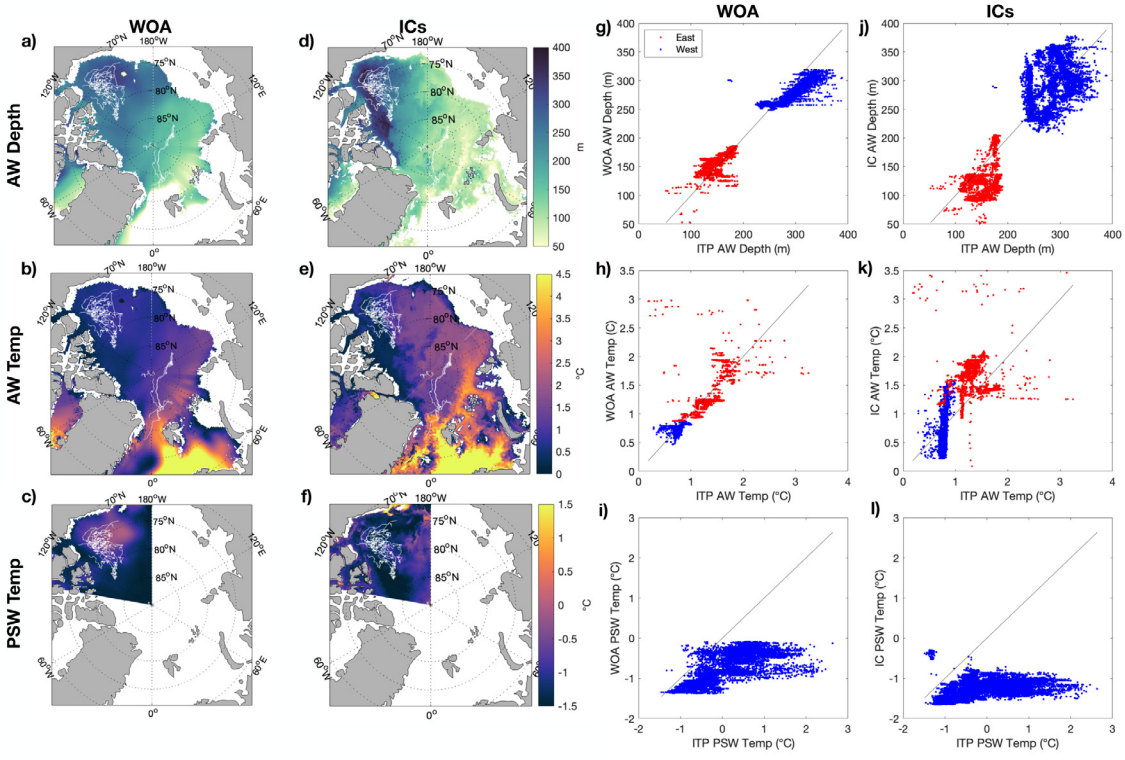

Fig. 3. Comparisons between the WOA18 (2005–2017) climatology (a,b,c) and UH8to2 initial conditions (ICs) (d,e,f), and ITP profiles (g through l) from 2017–2020 of (top) Atlantic Water Depth (m), (middle) Atlantic Water Temperature (°C), and (bottom) Pacific Summer Water temperature (°C). Panels g through l show direct comparisons between ITP-observed quantities and the value in the corresponding grid cell from the WOA (g,h,i) and UH8to2 ICs (j,k,l). ITP transects are shown as white lines in (a) through (f).

2.5.2. Heat content and ice melt potential

Heat content in the upper 100 m of the ocean is calculated as:

$$HC = \int_{100}^{0} \rho c_p (T - T_{ref}) dz \quad (1)$$

in which ρ is the density of seawater, taken as 1025 kg m^{-3}, c_p is the heat capacity of seawater, 4000 J °C^{-1} kg^{-1}, T is temperature in °C, and T_{ref} is the freezing temperature taken to be −1.9 °C. To provide physical intuition for the relevance of upper-ocean heat content, we convert heat content referenced to the freezing temperature to the

Table 2
Arctic gateway volume, freshwater, and heat transports. Standard deviations over the model run of each quantity are given in parentheses. Observed values are taken from a variety of studies (see footnotes); uncertainty ranges for observations vary depending both on site and on study methodology.

Quantity	Gateway	UH8to2	Observations
Volume (Sv)	Bering Strait	1.2 (1.1)	1.2 ± 1[a]
	Davis Strait	−2.1 (0.8)	−1.6 ± 0.5[b]
	Fram Strait	−1.6 (2.3)	−2 ± 2.7[c] −2 to −5[d]
	Denmark Strait	−5.2 (2.7)	−3.4[e]
	Barents Sea Opening	2.4 (1.4)	2.3[f]
Freshwater (mSv, ref 34.8 g/kg)	Bering Strait	88.2 (90.1)	95[g]
	Davis Strait	−132.4 (51.5)	−93 ± 6[h]
	Fram Strait	−101.45 (36.7)	−80 ± 6[i] (ref 34.92) −70 ± 24[j] (ref 34.9)
	Denmark Strait	−102.7 (52.2)	−65 ± 11[k] −108 ± 24[l]
	Barents Sea Opening	−8.5 (14.3)	6[m]
Heat (TW, ref -1.9 °C)	Bering Strait	17.2 (24.7)	13[n]
Heat (TW, ref -0.1 °C)	Fram Strait	39.5 (18.9)	28 ± 5 to 46 ± 5[o]
Heat (TW, ref 0 °C)	Davis Strait	13.6 (18.0)	20 ± 9[p]
Heat (TW, ref 0 °C)	Barents Sea Opening	70.6 (35.6)	~70[q]

[a]Woodgate (2018); [b]Curry et al. (2014); [c]de Steur et al. (2018); [d]Schauer et al. (2004); [e]Våge et al. (2013); [f]Smedsrud et al. (2013); [g]Woodgate (2018); [h]Curry et al. (2014); [i]Rabe et al. (2009); [j]de Steur et al. (2018); [k]Münchow et al. (2006); [l]Våge et al. (2013); [m]Segtnan et al. (2011); [n]Woodgate et al. (2012); [o]Schauer et al. (2004); [p]Curry et al. (2014); [q]Smedsrud et al. (2013)

quantity of sea ice it could melt if applied directly to sea ice at the freezing temperature, calculated as

$$IP = \frac{HC}{\rho_{ice} L_H} \tag{2}$$

in which ρ_{ice} is the density of ice, taken as 900 kg m^{-3} and L_H is the latent heat of melting, taken as 3.3×10^5 J m^{-3}. We refer to this quantity as the "ice melt potential".

3. Model realism

We begin by assessing the UH8to2 representation of the Arctic ocean-sea ice system, relative to historical observations, the WOA18 climatology, and synoptic satellite and ITP observations.

3.1. Model initial conditions relative to synoptic observations and climatology

We identified several differences between the ITP observations, the model initial conditions, and the WOA18 climatology. The ITP observations have warmer Pacific Summer Water than either the WOA18 climatology (Fig. 3c and i) or the model initial conditions (Fig. 3f and l). The WOA18 Pacific Summer Water is somewhat warmer and more variable in temperature than the model initial conditions, reaching temperatures of up to 0 °C but still significantly colder than observations which attain temperatures greater than 2 °C. ITP Atlantic Water depth and temperature is approximately the same as the WOA18 (Fig. 3g and h), while the initial condition Atlantic Water temperature is slightly warmer and shallower than ITP observations in the eastern Arctic (Fig. 3j and k). The model initial conditions also showed more Atlantic Water temperature variability in the western Arctic than seen in either the ITP observations or the WOA18 climatology (Fig. 3h and k). The model initial conditions had Atlantic Water that was slightly warmer than climatology (Fig. 3b and e). The differences between the ITP data and WOA18 climatology may indicate that the climatology deviates in some ways from the current state of the Arctic Ocean, which is changing rapidly. Note that while ITP data from 2017 was potentially available for assimilation into the 2005–2017 WOA product, the three more recent years were not. It also is possible that some of these differences are due to variability in the water masses that is suppressed in climatological averaging, particularly in the case of the Pacific Summer Water which is intermittently found throughout the basin.

3.2. Arctic gateway fluxes and circulation

Simulated volume, heat, and freshwater fluxes through major Arctic gateways generally agree well with observational estimates (Table 2). Volume and freshwater fluxes are given for the Bering, Fram, Davis, and Denmark Straits, and for the Barents Sea Opening. Heat fluxes are given for the Bering, Fram, and Davis Straits, as well as for the Barents Sea Opening, where recent observational estimates are available. Model mean transports are within a standard deviation of observational estimates and usually within reported error bounds of observations where such error bounds are available, with the caveat that the observations generally date from earlier periods than the model run. Atlantic Water biases within the basin (discussed in more detail in Section 3.3) motivated a more detailed comparison of Fram Strait temperature and velocity with the Alfred Wagner Institute moorings that were deployed across Fram Strait in 2017 and 2018 (not shown). While there were minor differences between the model and the mooring observations, both the temperature and dynamical structure agreed well with observations (von Appen, 2019; von Appen et al., 2019). The model's northward velocity core was more zonally diffuse; ~1 km horizontal resolution modeling studies suggest this may be an artifact in our model due to insufficient horizontal resolution (Wekerle et al., 2017). Sections through the other gateways suggested generally good agreement between the modeled and observed current pathways and temperature/salinity structure (not shown).

Modeled Arctic velocity fields (Fig. 4) reproduce the major features of Arctic circulation, including the cyclonic boundary circulation originating in Fram Strait, the anticyclonic Beaufort Gyre, and the transpolar drift (Rudels et al., 2004; Armitage et al., 2017; Nguyen et al., 2021). 2017 UH8to2 surface velocities are in a similar range to velocity estimates from the 2017 ASTE (Nguyen et al., 2021), although velocities are somewhat larger and show more eddy variation, likely due to the higher resolution of the UH8to2 model allowing more developed mesoscale dynamics. Modeled velocities in the central Arctic

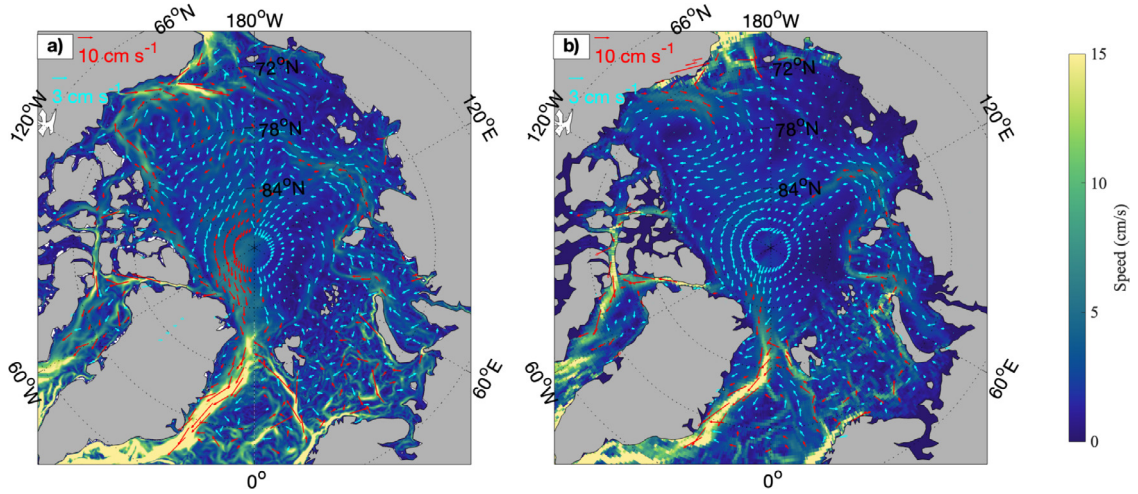

Fig. 4. 2017 Arctic surface velocities (cm s^{-1}) from (a) the UH8to2 model and (b) the ASTE estimate (Nguyen et al., 2021). The ASTE estimate was interpolated onto a 0.3 degree grid in latitude and longitude for this comparison.

were modest (a couple centimeters per second), except in boundary currents at the basin's margin and along the Chukchi slope (north of Alaska), where they at times exceeded 10 cm/s. The model successfully captured intricate flow fields in the Chukchi Sea and Fram Strait. Warm eddies and intrusions (not shown) were apparent associated with Bering Sea inflow, similar to observed small-scale features (Fine et al., 2018; MacKinnon et al., 2021).

3.3. Sea ice

Sea ice mediates exchanges of heat, fresh water, and momentum between the atmosphere and ocean, and is itself impacted by both atmospheric and oceanic forcing. Monthly total sea ice extent (Fig. 5a and b), defined as the sum of the area of the grid cells in which sea-ice concentration is greater or equal to 15%, is compared between the UH8to2 simulation and from a compilation of satellite observations for 2017–2020. In December through February, UH8to2 total sea ice extent closely follows observations, with the simulated and observed February maximum sea ice extent agreeing well. In March through June, the UH8to2 values are slightly larger than observed, while in August through October the simulated total sea ice extent is significantly lower than observed values. The UH8to2 mean September minimum is roughly 1.5 $\times 10^6$ km^2 or 1.8 $\times 10^6$ km^2 lower than that obtained from the bootstrap or NASA Team algorithms, respectively. Using the standard error from each of the bootstrap and NASA Team time series to define the 95% significance level, the spring excess was only significant in May and June of 2018 and 2020, while UH8to2 values lie outside of the observational error bounds in August through October of all years.

Over 2017–2020, satellite observations found a negative trend in total sea ice extent (Fig. 5c). This trend was represented well by the UH8to2 model, with the model trend lying between the two different estimates from the NASA and bootstrap algorithms. Anomalies from the seasonal means were also captured well by the model, with only small differences between the modeled and observed anomalies.

Similarly, maps of monthly-averaged sea ice concentration (Fig. 6; over areas with at least 15% concentration) shows good agreement with SSM/I observations in April of 2020, however as the year progresses model ice is lost too quickly relative to observations. By June 2020, the ice edge is realistic but concentrations are about 10% lower in the Pacific sector and in parts of the Eurasian basin south of 80° N. In September 2020, the UH8to2 ice edge has retreated further than in satellite observations, and ice concentration over the modeled ice cap is too low. In October 2020, UH8to2 concentrations are largely in agreement with observations but the ice edge is still somewhat less extensive in the central Arctic than in observations. By November 2020, the ice extent is very realistic but sea ice concentrations are biased low in the Eurasian basin south of 80° N. These biases appear in all years, but are most dramatic in 2020, which had the lowest summer sea ice extent of all four years in both the model and observations.

Monthly sea-ice thickness from the UH8to2 model and CryoSat −2 show simulated sea-ice thicknesses that are generally thinner than observed (Fig. 7). October 2019 through March 2020 are shown, as biases in thickness increased during the four year model period, and this was the last full winter over which the simulation was run. These differences are especially pronounced in October through December. In these months, observed ice is thicker over the entire ice cap by 0.5–2.0 m, except for a slim band north of Greenland where the model is up to 0.5 m thicker. The largest discrepancies occur in the central and eastern Arctic. In February through March 2020, simulated sea-ice thicknesses are about 0.5–1.0 m thinner than the observations in the central Arctic and Eurasian basins, whereas in the western Arctic and just to the north of the Canadian Archipelago the model fields are about 0.25–0.5 m thicker. Biases are at a minimum in January. The low thickness biases in the model from October through December indicate a delay in the freeze cycle relative to observations in the Eurasian Basin and central Arctic. CryoSat −2 thickness estimates agree with *in situ* observations with errors in the range of 0.5–10 cm, however, errors in radar retrieval can be as large as 40 cm (Giles et al., 2007; Center for Polar Observation and Modelling Data Portal, 2023)

In summary, UH8to2 sea ice shows a realistic seasonal cycle and accurately captures anomalies over the four year model run, however it tends to be biased towards low sea ice extent and concentration in summer months and low thickness in winter months. These biases occur throughout the Arctic with the exception of the region just north of Greenland and the Canadian Archipelago, and are most dramatic in the central and eastern Arctic, where winter thickness is particularly reduced.

3.4. Hydrography

Due to the Arctic Ocean's salinity-dominated stratification, hydrographic structure determines where oceanic heat is stored in the basin and how accessible it is to the surface. In this section we examine the model representation of the major reservoirs of subsurface Arctic heat, Atlantic Water and Pacific Summer Water, as well as the model's representation of near-surface stratification. These oceanic features play a key role in determining how subsurface water masses influence ice-ocean processes. We contrast the model's representation of these water masses to the WOA18 climatology and synoptic ITP profiles.

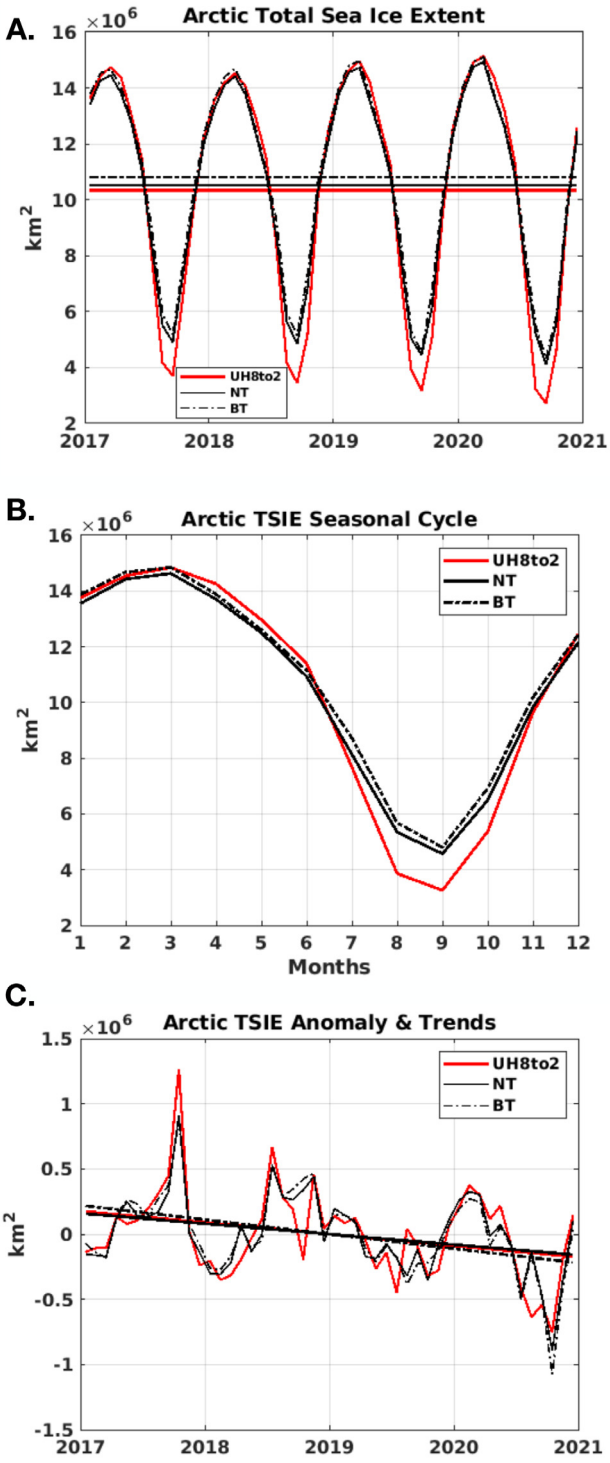

Fig. 5. (a) Monthly total sea ice extent (TSIE, sum of the sea-ice area in which sea-ice concentration is greater or equal to 15%, units of km^2) from the UH8to2 simulation, satellite observations using the NASA Team (NT) algorithm, and bootstrap algorithm (BT); (b) seasonal cycle of TSIE averaged over the 2017–2020 UH8to2 run; (c) TSIE seasonal anomaly and trend over 2017–2020.

3.4.1. Arctic hydrographic structure

A vertical section through the Arctic Ocean, chosen to sample the major Arctic water masses, was compared between the four-year averaged UH8to2 model and WOA18 climatology (Fig. 8). Both the climatology and the model output show a halocline-stratified Arctic Ocean, with consistent regional patterns. The eastern Arctic is warmer and saltier, while the Beaufort gyre-influenced western Arctic is cooler and fresher, with the transition between basins occurring near the north pole at the Lomonosov ridge. Subsurface Atlantic Water appears in both the UH8to2 model and WOA18 climatology, and is shallower and warmer in the eastern Arctic than in the west.

Differences between the UH8to2 model and climatology become apparent in this comparison as well. The UH8to2 Atlantic Water is warmer than in the WOA18 climatology in both the western and eastern Arctic (Fig. 8a, b and c). The UH8to2 model additionally lacks the subtle sub-surface temperature maximum between 40–100 m depth in the western Arctic associated with Pacific Summer Water (Timmermans et al., 2014). The strength of the halocline stratification also differs between the model and climatology, with the UH8to2 model exhibiting a saltier surface and fresher subsurface in the upper 100 m of the western Arctic (Fig. 8d, e and f), where Ekman convergence associated with the Beaufort Gyre results in a concentration of surface fresh water (Proshutinsky et al., 2019). As salinity controls stratification in this region, a weaker salinity gradient in the UH8to2 model results in reduced stratification in the upper ocean relative to the WOA18 climatology. These differences, and their implications for heat storage and transport in the modeled Arctic, will be explored further in the following sections.

During the years of the model run, 25 ITPs were deployed in the Arctic Ocean, primarily in the western Arctic (Table 1), providing a basis for comparing the UH8to2 model with concurrent observations. We approach this comparison in two ways: first, instantaneous ITP observations are compared to mean model fields. For this comparison, we use the four year mean for modeled Atlantic Water depth, Atlantic Water temperature, and Pacific Summer Water temperature, and the four year mean over January through March of the model mixed layer depths (Fig. 9). This method allows for us to understand the ITP observations in the context of larger scale spatial patterns, with the disadvantage that we compare instantaneous observations with mean model fields. As a second approach, we compare observed ITP profiles with the daily average model characteristics at the time and location the ITP profile was initiated. While this still necessitates comparing a pointwise observation with a model value from a finite-sized grid cell and over a daily average, the sampling strategy between the observed and modeled ocean is much more similar. We consider "average profiles" over the eastern and western Arctic across both the modeled and observed ITP deployments (Fig. 10). We additionally note that multiple factors may contribute to differences between observed and modeled profiles; for instance, ice may be present at the location of an observed ITP profile but absent in that model location, or vice versa. However, larger-scale hydrographic patterns are consistent across both methods of model-observation comparison.

3.4.2. Atlantic Water

Considering the basin-wide signatures of Atlantic Water in the UH8to2 model compared to the WOA18 climatology (Fig. 11), we find that Atlantic water is shallower (Fig. 11a and d), warmer (Fig. 11b and e), and saltier than in the climatology (Fig. 11c and f). Here 2020 annual averages are compared to the climatology, as biases were largest in this year. These discrepancies appear throughout the Arctic. Some of these differences may be attributable to ongoing climate change; one of the signals of climate change is a warming Arctic, and the increased heat and salinity contained in Atlantic water has been previously documented (Polyakov et al., 2017, 2018). Observational data used to create this climatology may not reflect the very recent conditions of this model run as the WOA18 uses observations from 2005–2017. To determine whether this is a true model bias or an accurate reflection of continuing climate change, we compare the UH8to2 model with available ITP observations from the years over which the model was run.

The four-year averaged UH8to2 Atlantic Water is also shallow and warm relative to the ITP observations (Fig. 9e and f and Fig. 10a

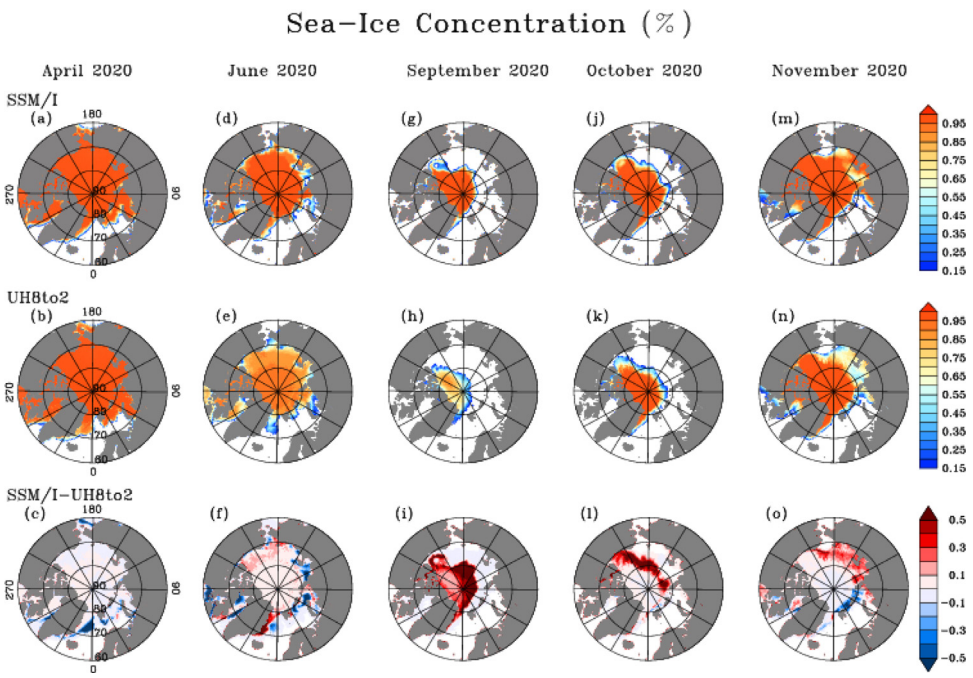

Fig. 6. Fractional sea ice concentration over areas with at least 15% ice concentration from SSM/I (top) and UH8to2 (bottom) in April (a and b), June (d and e), September (g and h), October (j and k), and November (m and n) of 2020. Differences between SSM/I and UH8to2 values are shown in panels c, f, i, l, and o.

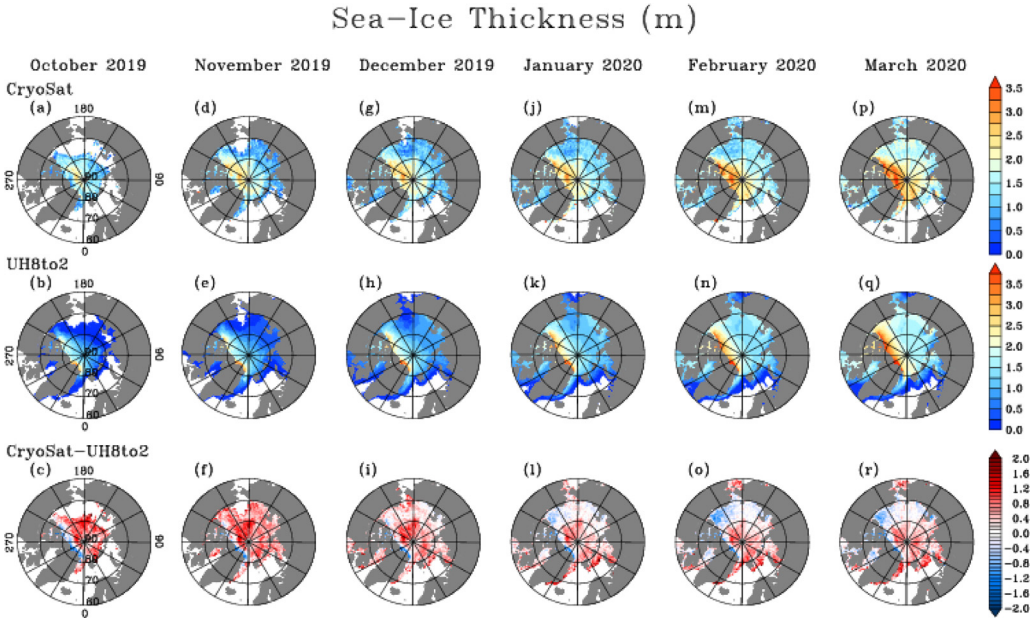

Fig. 7. Sea ice thickness (m) for Cryosat −2 (top), UH8to2 (middle), and their difference (bottom) in October 2019 through March 2020 (left to right).

and b). The smallest temperature biases are observed in the western Arctic. Here observations find Atlantic Water around 300 m depth, while it is generally shallower in the UH8to2 model, around 250 m. Temperature discrepancies between the model and observations are approximately 0.5 °C. In the eastern Arctic, UH8to2 Atlantic Water is shallower, 100–150 m beneath the surface, with observations in the 150–200 m range. Mean temperature discrepancies between the model and observations in the eastern Arctic are over 1 °C, and discrepancies of >2 °C are sometimes observed. This bias was apparent in the model initial conditions (suggesting that a different initialization procedure potentially could have led to a different outcome) but worsened over time, with the biggest discrepancies occurring later in the model run (not shown). A full investigation into the source of this bias is beyond the scope of this work.

3.4.3. Pacific Summer Water

In much of the literature, Pacific Summer Water is described as an intermittent temperature maximum of around −0.5 to 0 °C (Shimada et al., 2001; Steele et al., 2004; Timmermans et al., 2014, 2018). In the WOA18 climatology this temperature maximum appears, but is quite subtle (Fig. 8b). However, in the synoptic ITP data from 2017–2020, September Pacific Summer Water temperatures are frequently over 0 °C (Fig. 9g), significantly warmer than the four-year model September mean (September is chosen for this comparison as the maximum model

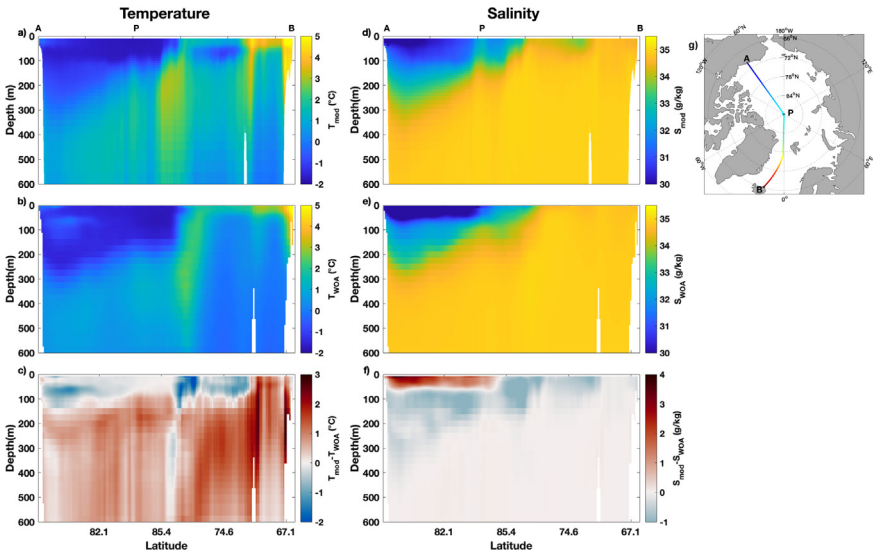

Fig. 8. Cross-Arctic sections of (a) four-year average UH8to2 temperature (°C), (b) WOA18 (2005–2017) temperature (°C), (c) four-year average UH8to2 and WOA18 (2005–2017) temperature difference (°C), (d) four-year average UH8to2 salinity (g kg^{-1}), (e) WOA18 (2005–2017) salinity (g kg^{-1}), and (f) four-year average UH8to2 and WOA18 (2005–2017) salinity difference (g kg^{-1}), with (g) overhead view of the cross-Arctic section. Panels (a) through (f) are oriented so that the western Arctic (north of Canada) is on the left hand side of the panel.

Table 3
Mixed layer depths in the eastern and western Arctic, during winter and summer months. Mixed layer depths are given in m, with standard deviations in parentheses.

	Western Arctic Winter	Western Arctic Summer	Eastern Arctic Winter	Eastern Arctic Summer
Observed ITPs	46 (7)	28 (14)	43 (9)	27 (7)
Model ITPs	85 (10)	27 (9)	77 (5)	33 (10)

Pacific Summer Water temperatures occur in September). Mean temperature profiles from the western Arctic ITP profiles show a distinct peak in temperature around 65 m depth (Fig. 10a). In contrast, the model output lacks a significant Pacific Summer Water temperature maximum, with maximum temperatures in this depth range in the western Arctic usually less than −1 °C even in September (Fig. 9c and g). There is no subsurface temperature maximum in the mean western Arctic UH8to2 temperature profile shallower than the depth range of the Atlantic Water (Fig. 10a).

3.4.4. Mixed layers

Arctic mixed layers are shallow in summer as ice melt increases near-surface stratification, and deepen in winter due to storm-driven wind forcing and brine rejection as the ice cover freezes (Peralta-Ferriz and Woodgate, 2015). As mixed layers deepen in winter, heat in the warm Pacific and Atlantic water masses may be entrained into the surface layer. Winter mixed layer depths in the model are generally deeper than ITP observations, particularly in the western Arctic (Fig. 9d and h, Table 3), with discrepancies of 20–40 m. Histograms of winter mixed layer depth from observed and modeled ITP profiles show clear separation between the modeled and observed winter mixed layers in both the eastern and western Arctic (Fig. 12a,b). The mean observed winter mixed layer depth in the western Arctic is 46 m (standard deviation 7 m), while the winter mean modeled mixed layer depth in the western Arctic reaches 85 m (standard deviation 10 m). There is a similar but slightly smaller discrepancy in the eastern Arctic, with an observed winter mixed layer mean of 43 m (standard deviation 9 m) and a modeled mean of 77 m (standard deviation 5 m). During the summer, this discrepancy vanishes, with modeled and observed means agreeing to within 10 m in both the eastern and western Arctic.

To summarize, in examining both climatologies and simultaneous ITP data, we find that the UH8to2 modeled water column has a realistic structure, with halocline stratification, a persistent Atlantic Water temperature maximum, and is fresher and cooler in the western Arctic compared to eastern basin (Fig. 8). Some biases in the UH8to2 simulation are observed and are similar in magnitude to those found in other Arctic models discussed in the Introduction. In particular:

- Modeled UH8to2 Atlantic Water is warmer and shallower than in both the WOA18 climatology and ITPs, particularly in the eastern Arctic. (Figs. 8, 11, 9, and 10).
- The model is largely lacking Pacific Summer Water, which appears as a striking temperature maximum in ITP observations (Figs. 8, 9, and 10).
- Model winter mixed layers are deeper than in observations, particularly in the western Arctic. This discrepancy is associated with a generally weaker salinity gradient, leading to lower upper-ocean stratification (Figs. 8, 9 and 12).

In the next section we examine the implications of these biases for ice-ocean interactions.

4. Ice-ocean interactions

The Arctic climate is potentially sensitive to positive feedbacks between the ice and ocean, as described in the Introduction. These feedbacks are all associated with oceanic heat fluxes which excessively melt sea ice, leading to further consequences for the ice–ocean–atmosphere system. Thus, a key goal of this work is to understand how the ocean model biases identified in hydrographic structures impact ice-ocean heat fluxes. The potential for oceanic heat to impact sea ice is greatest in the winter, when mixed layers deepen so that ocean interior properties can directly affect the surface. In the four-year monthly averages, ice grows during the winter due to strong atmospheric cooling, and melts during the summer as both the ocean and atmosphere provide heat to the ice (Fig. 13; note that in the upper panel curves stack). During the summer melting season, melting is about equally partitioned

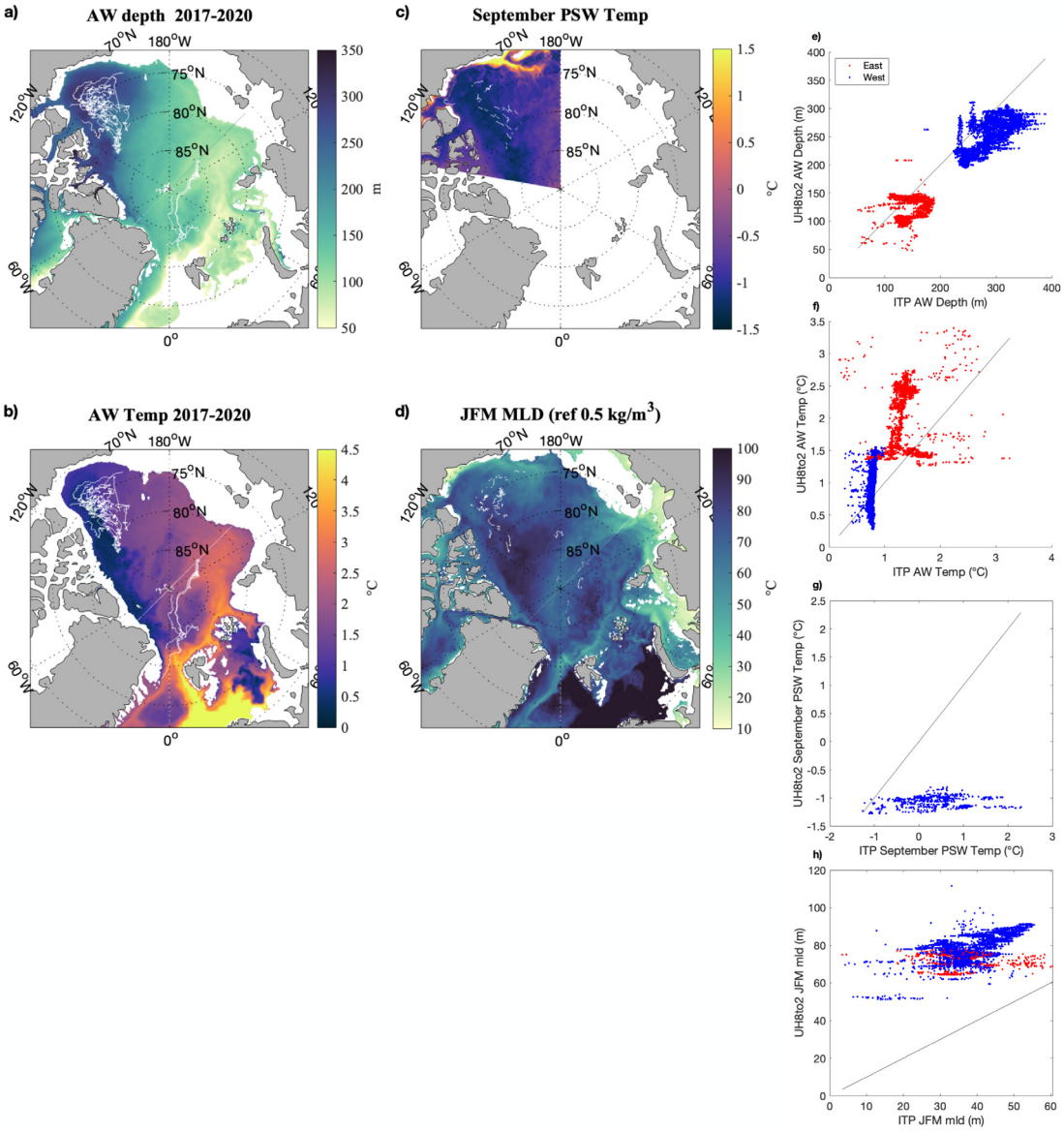

Fig. 9. Comparison of four-year averaged UH8to2 and ITP-observed quantities. (a) UH8to2 Atlantic Water depth (m) from 2017–2020, (b) UH8to2 maximum Atlantic Water temperature (°C) from 2017–2020, (c) UH8to2 Pacific Summer Water temperature (°C) in September of 2017–2020, and (d) UH8to2 winter (January, February, and March) mixed layer depths (m) from 2017–2020. (e) through (h) show comparisons of ITP-observed values of each quantity with the UH8to2 value in the 0.25 ° interpolated grid, where eastern deployments are in red and western in blue. ITP transects are shown as white lines in (a) through (d).

between top and bottom melt (Fig. 13a, c, and e). However, even in the winter months there is a modest loss of sea ice due to bottom melt. This effect is particularly strong in the eastern Arctic (Fig. 13a). Considering heat fluxes to the ice, we see the atmosphere generally acts to cool the ice, with the exception of the months of June and July, when the atmosphere provides a positive heat flux to the ice (Fig. 13b, d, and f). Conversely, the ocean is always a source of heat to the ice, with peak ocean warming occurring in the summer, when thin or patchy ice allows for insolation of the upper ocean, which can then transfer heat to the sea ice. However, a smaller local maximum in the ocean warming occurs during the winter months. Once again this effect is strongest in the eastern Arctic, with ocean–ice heat fluxes exceeding 10 W m^{-2} in January and February (Fig. 13b). It is this winter oceanic heating of sea ice that is likely to be most sensitive to discrepancies in the ocean interior. A warmer upper ocean, combined with deeper winter mixed layers, leads to increased quantities of oceanic heat available to the deepening winter mixed layer. Heat within the mixed layer is then available to melt or reduce growth of winter sea ice, so that oceanic biases may cause biases in model sea ice volume and extent, as appear in comparisons between the UH8to2 ice representation and satellite observations (Figs. 5, 6, and 7).

The ice–ocean–atmosphere system is complex and includes mechanisms for both positive and negative feedback, so that there are many possible causes of these biases. However, the aim of this section is to examine the potential impact of the wintertime oceanic processes that regulate sea ice growth and melt in the model relative to observations in order to better understand the climate implications of the oceanic biases discussed in Section 3.4. We begin by considering representative ITP deployments in the eastern and western Arctic over the winter season. These deployments demonstrate the seasonal changes in upper-ocean heat content, stratification, and mixed layer depth in each basin.

4.1. Seasonal evolution of the upper ocean in ITP deployments

Example ITP deployments show two separate scenarios for how biases in the UH8to2 fields influence representations of ice-ocean heat

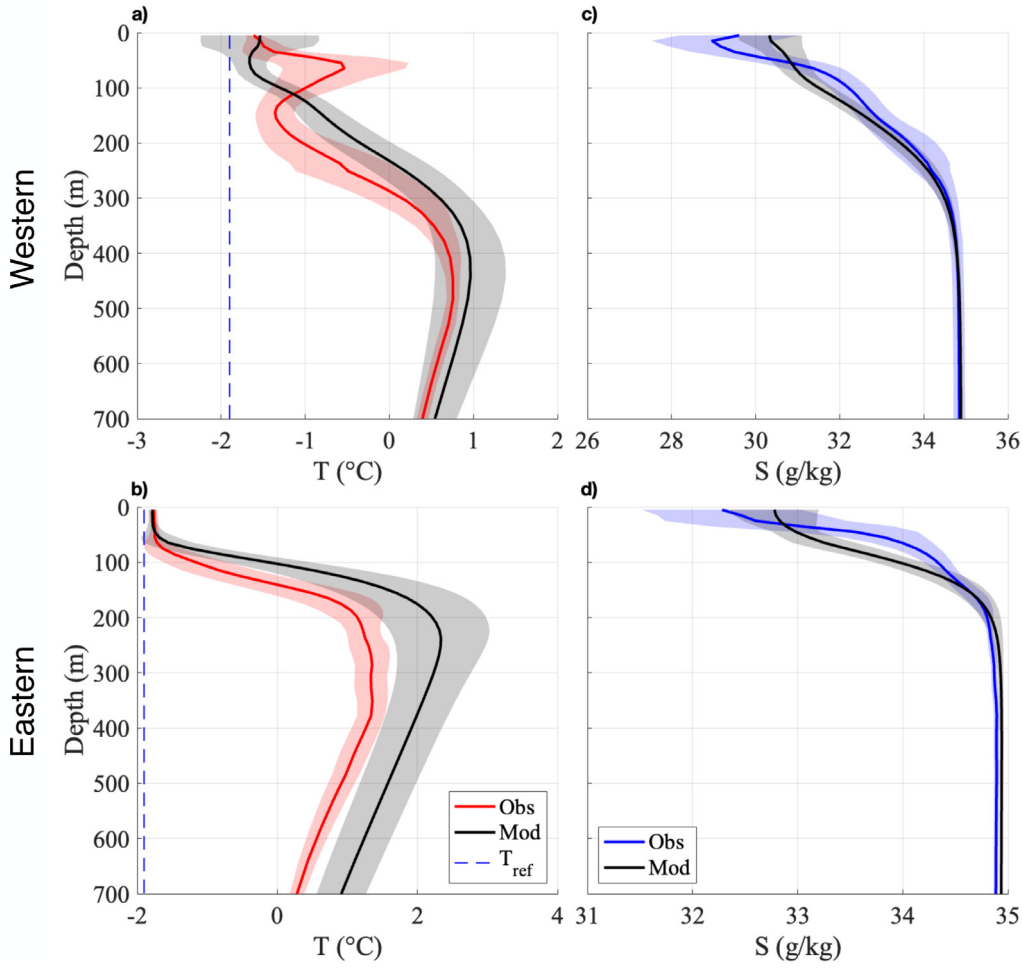

Fig. 10. Comparison of mean ITP-observed profiles (red and blue) and matched synoptic model profiles (black) of (a) temperature (°C) in the western Arctic (latitudes between 0 and 180 °W), (b) temperature (°C) in the eastern Arctic (latitudes between 0 and 180 °E), (c) salinity (g kg^{-1}) in the western Arctic (latitudes between 0 and 180 °W), and (d) salinity (g kg^{-1}) in the eastern Arctic (latitudes between 0 and 180 °E). Shaded regions represent a standard deviation around the mean. T_{ref} is the reference freezing temperature of −1.9 °C. In total the ITP record includes 4218 profiles in the east and 35724 profiles in the west.

flux as mixed layers deepen during winter in the eastern and western Arctic. A deployment in the eastern Arctic (ITP #111) shows differences between the model and observed ITP deployment (Fig. 14). In both the observed and UH8to2 deployment, a surface mixed layer near the freezing temperature deepens in October through April (Fig. 14b and c). In the observations, this cold mixed layer (red line) lies above a cold halocline layer, with more stratified water beneath the mixed layer still near the freezing temperature. This cold halocline layer extends from the mixed layer to about 100 m depth, and separates the deepening mixed layer from the heat contained in warm Atlantic Water (Fig. 14e). In the UH8to2 deployment, the cold mixed layer is initially deeper than the observed mixed layer, and reaches greater depths as the winter progresses (Fig. 14c and f). While there is some stratified cool water beneath the mixed layer, this modeled cold halocline is very thin (Fig. 14f). Additionally, the UH8to2 Atlantic Water is warmer than observed (Fig. 14c). These discrepancies suggest that the cold halocline structure which serves as a barrier to prevent entrainment of Atlantic-origin heat into the mixed layer is likely less effective in the model, potentially allowing increased mixed-layer heat entrainment.

In an example western Arctic deployment (Fig. 15, ITP #114), observed mixed layer depths show a similar discrepancy with the UH8to2 model as seen in the eastern Arctic deployment of ITP #111, with deeper UH8to2 mixed layers in October, which proceed to deepen further in the winter (Fig. 15b and c). However, the water column structure in the western ITP #114 deployment is different from the eastern ITP #111. In ITP #114 observations, the Pacific Summer Water temperature maximum is clearly apparent at depths of 50–75 m (Fig. 15b). In the UH8to2 deployment, much less heat is found at these depths (Fig. 15c). By April the UH8to2 mixed layer reaches depths of 100 m, and is near the freezing temperature, suggesting that any heat above 100 m was entrained into the deepening winter mixed layer. The UH8to2 deployment additionally shows very low stratification above this depth compared to the observations (Fig. 15e and f). While there is more heat above 100 m in the observed temperature section, which could potentially be entrained into the mixed layer, the observed mixed layer never deepens into the stratified Pacific Summer Water temperature maximum. Thus model biases in the western Arctic deployment #114 could lead to either increased or diminished heat flux from the ocean to overlying ice, as the model does not retain the year-round temperature maximum seen in observations.

4.2. *Upper-ocean heat and freshwater content*

Comparing ITP observations with synoptic model profiles in both the eastern and western Arctic suggests that the patterns observed in the individual deployments of ITPs #111 and #114 are robust. Here we consider mean temperature and salinity profiles in the ocean shallower than 100 m, below which oceanic properties show little seasonal variation, in October and March (Fig. 16). These months were chosen as representative of the start and end of the freezing period. A caveat in the eastern Arctic is that while numerous profiles were collected in

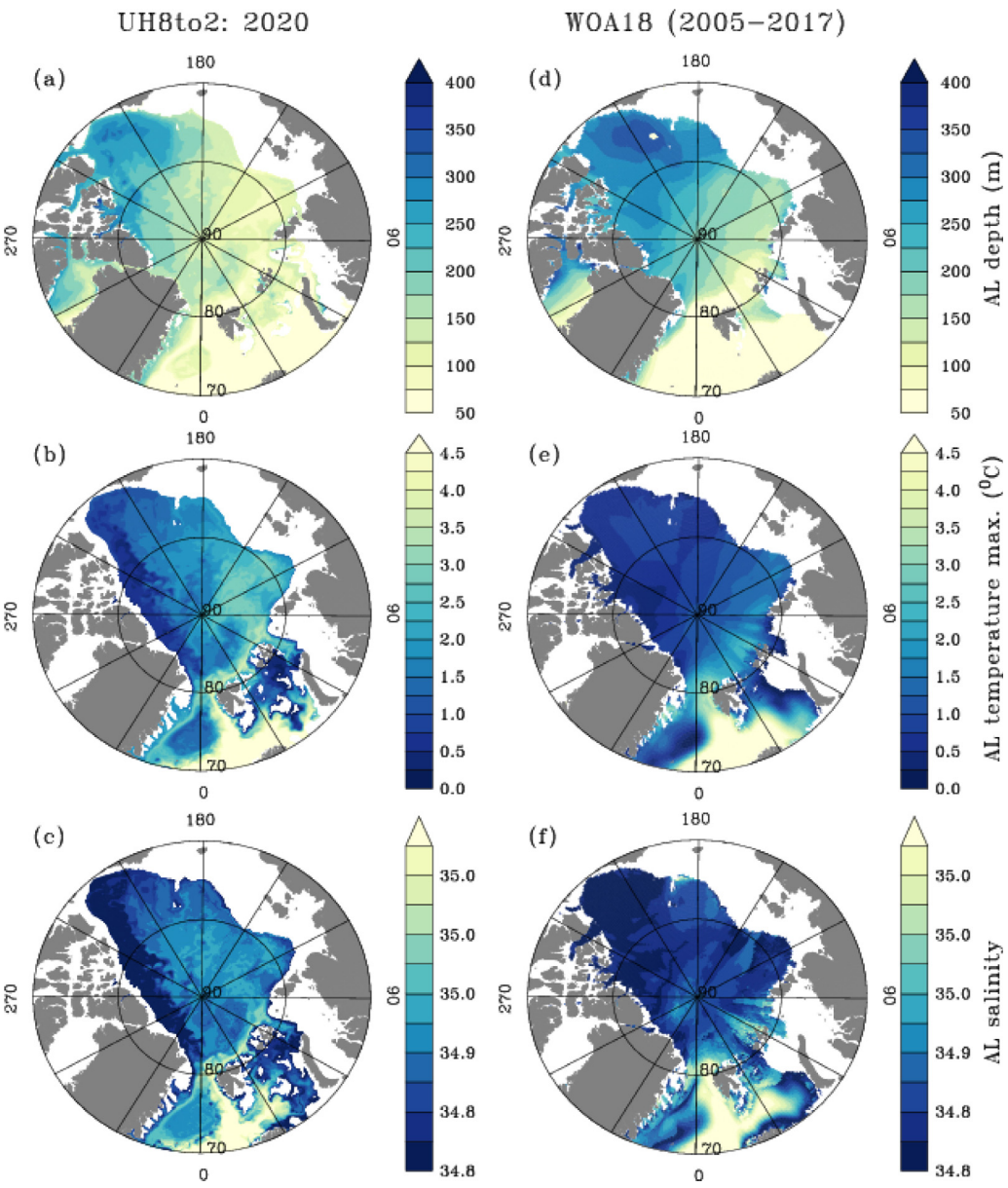

Fig. 11. Atlantic layer characteristics in the UH8to2 (year 2020) and WOA18 (data from 2005–2017). Top: depth (m), defined as the upper-most depth in the water column below 50 m of the 0 °C isotherm for (a) UH8to2 (2020) and (d) WOA18. Middle: maximum temperature (°C) in the Atlantic layer located between the subsurface 0 °C isotherms where salinities are greater than 34.8 for (b) UH8to2 and (e) WOA18. Bottom: salinity at the depth of the temperature maximum from (c) UH8to2 and (f) WOA18.

each season, the spatial distribution of sampling was strongly biased, as three ITPs were released in the central Arctic in the late summer and then drifted toward Fram Strait over the following months, so that temporal differences cannot be examined without also considering the influence of spatial inhomogeneity. However, persistent patterns occur, as follows.

In the eastern Arctic, we find that the warmer and shallower UH8to2 Atlantic Water results in warmer October temperatures in the upper 100 m relative to ITP observations (Fig. 16a). The UH8to2 salinity has a weaker gradient in the model relative to observations (Fig. 16e). In March, the difference between observed and modeled mean temperature profiles is much smaller, as both have a mixed layer near the freezing temperature that extends to 80 m depth (Fig. 16b). The discrepancy between UH8to2 and observed salinity is smaller in March than in October, with a saltier observed mixed layer (Fig. 16f). In the western Arctic, we find a more persistent temperature difference between the UH8to2 model and ITP observations, as the Pacific Summer Water temperature maximum centered around 60 m depth is seen in both October (Fig. 16c) and March (Fig. 16d) observations, but absent in the UH8to2 profiles (Fig. 16 c and d). This temperature maximum is associated with a persistent halocline (Fig. 16g and h), although the observed mixed layer is more saline in March than in October. In observations, the cold winter mixed layer in the Western Arctic only reaches about 40 m depth. Conversely, the UH8to2 model lacks the Pacific Summer Water temperature maximum, and has a much deeper winter mixed layer, which extends to approximately 80 m depth. Salinity gradients are weaker in the UH8to2 model than in ITP observations; the model also lacks the Pacific halocline.

These differences lead to discrepancies in upper-ocean heat content between the UH8to2 model and ITP observations (Table 4). Upper-ocean heat content has the potential to melt significant amounts of sea ice in both the observed and modeled profiles (Table 5, see Methods). Considering the integrated heat content above 100 m in the eastern Arctic, we find more upper-ocean heat in the UH8to2 model than in the observations, associated with a warmer and shallower Atlantic Water temperature maximum. The UH8to2 heat content would be sufficient

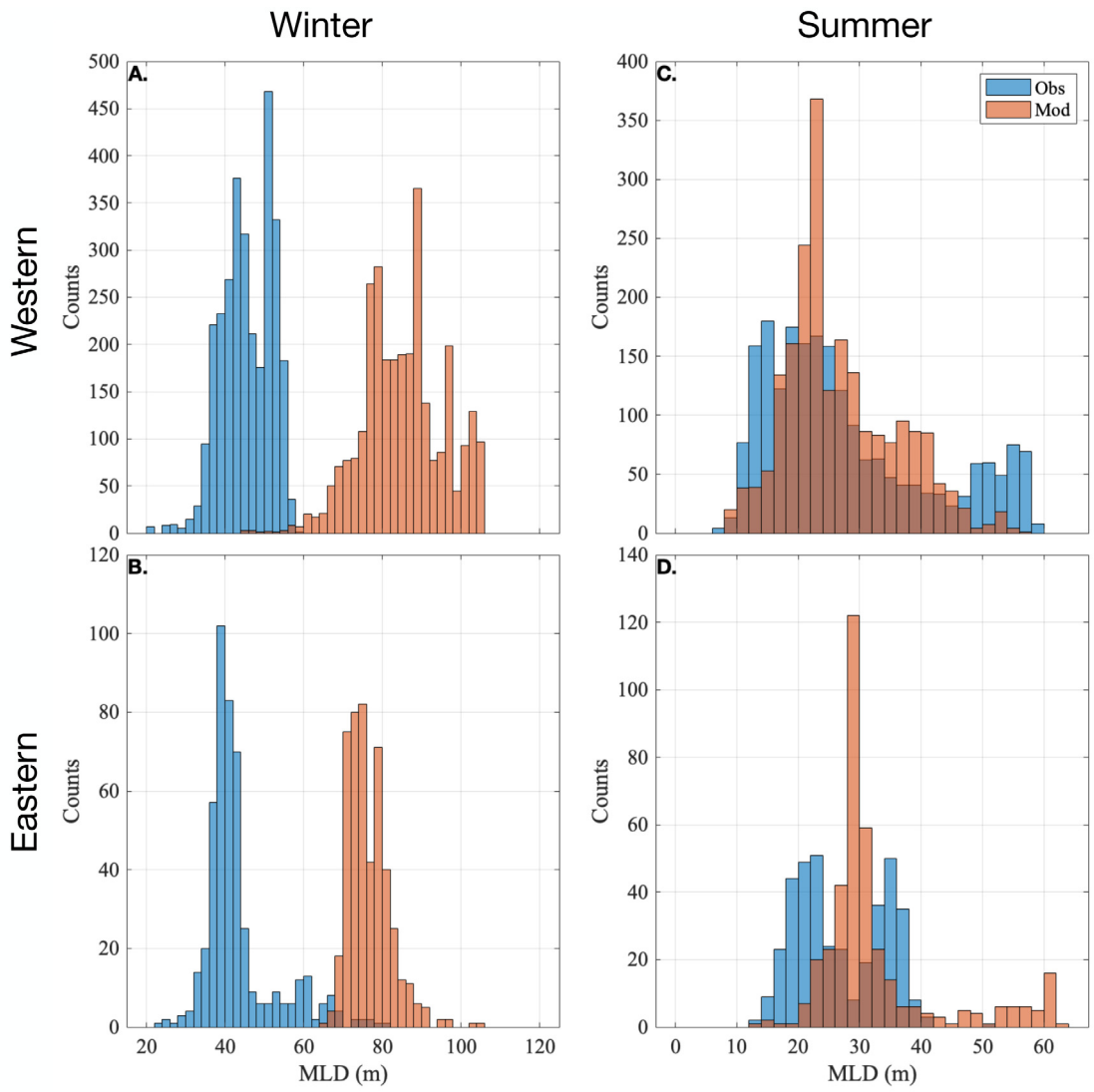

Fig. 12. Histograms of mixed layer depths (m) compared between ITP observed profiles (blue) and synoptic model profiles (red) for (a) winter (January, February, and March) in the western Arctic, (b) winter in the eastern Arctic, (c) summer (July, August, September) in the eastern Arctic, and (d) summer in the eastern Arctic.

Table 4
Heat content in the upper 100 m of the eastern and western Arctic, mean values for October and March. Heat content is given in units of 1×10^7 J m^{-2}.

	Eastern October	Eastern March	Eastern Difference	Western October	Western March	Western Difference
Observed ITPs	9.8	4.6	5.2	36	27	10
Model ITPs	18	6.1	12	14	5.1	8.9

Table 5
Ice melt potential of the heat content of the upper 100 m of the eastern and western Arctic, mean values for October and March. Ice melt potential is given in units of cm m^{-2}.

	Eastern October	Eastern March	Eastern Difference	Western October	Western March	Western Difference
Observed ITPs	33	15	18	121	90	31
Model ITPs	62	21	41	48	17	31

to melt 62 cm of ice per m^2 of surface area if it were brought entirely to the ocean surface, while the observed heat content could melt only 33 cm of ice per m^2. In both the UH8to2 and observed deployments, more heat is found in October, when the cool mixed layer is shallower (~30–40 m) compared to March, when the mixed layer is around ~80 m depth. However, the difference in heat content between October and the following March is bigger in the UH8to2 mean relative to observations. In the model, the change in heat content from October to March would be sufficient to melt 41 cm of ice per m^2, while the observed difference in heat content could only melt 18 cm of ice per m^2. This supports the hypothesis that the relatively warm and shallow Atlantic layer in the model results in increased entrainment of oceanic heat into the mixed layer, potentially weakening the winter sea ice in the eastern Arctic.

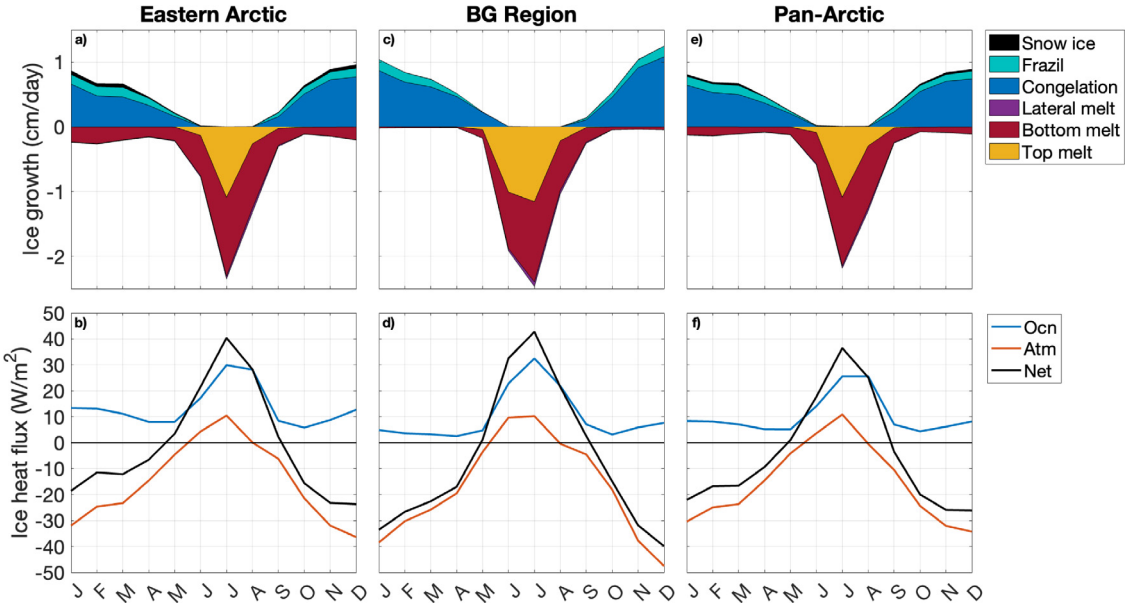

Fig. 13. UH8to2 four-year monthly average sea ice growth in m (a, c, e; curves stack so that the shaded area represents the value of each term) and heat flux in W m^{-2} (b, d, f) budgets for the eastern Arctic (a and b), Beaufort Gyre region (c and d) and pan-Arctic Ocean (e and f). Signs for atmospheric and oceanic heat fluxes are chosen so that a positive flux represents heating of the ice. Here the "Beaufort Gyre region" is defined as all grid cells between longitudes of 180 and 120° W and north of 70° N; "eastern Arctic" is grid cells between longitudes of 0 and 160° E and north of 80° N; and the "pan-Arctic Ocean" is all grid cells north of 80° *N* along with those grid cells east of 90° E and west of 90° W which are north of 70° N.

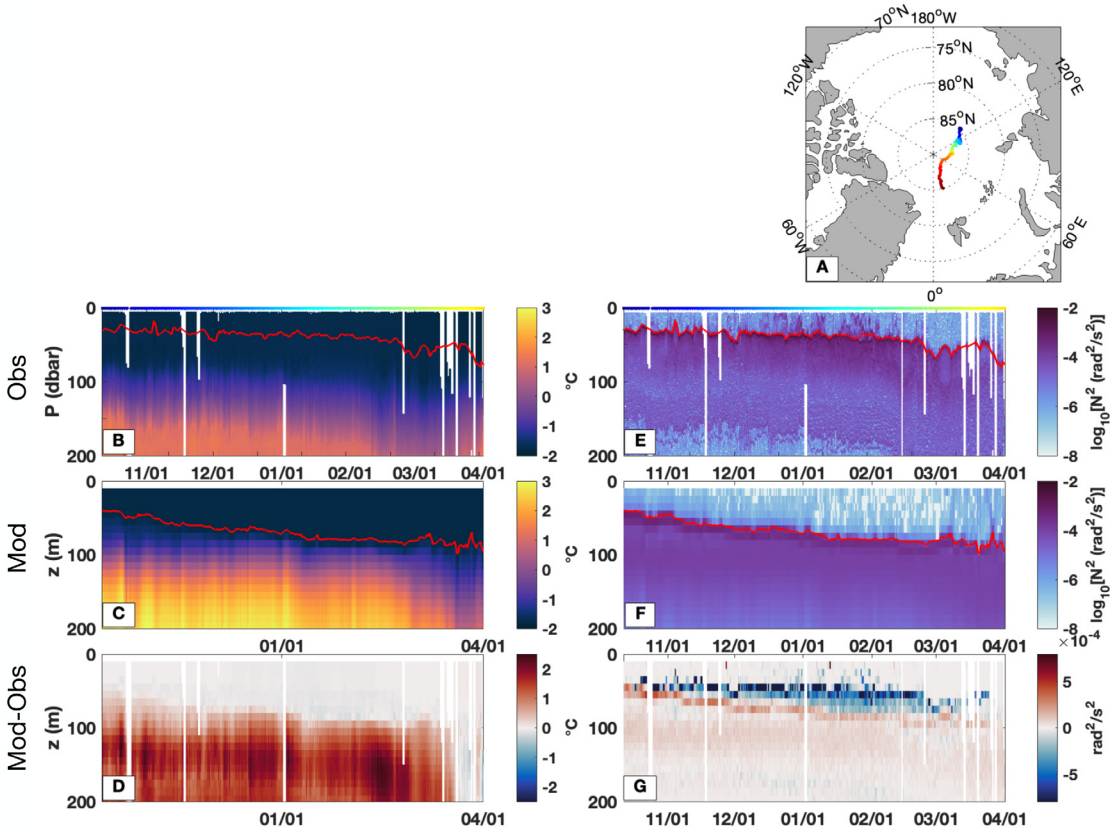

Fig. 14. ITP #111 section in the eastern Arctic. (a) Overhead map of ITP deployment, (b) observed temperature (°C), (c) modeled temperature (°C) along ITP deployment, (d) model-observed temperature difference (°C), (e) observed buoyancy frequency (rad^2 s^{-2}), (f) modeled buoyancy frequency (rad^2 s^{-2}), (g) model-observed buoyancy frequency difference (rad^2 s^{-2}). The mixed layer depth is shown as a red line in panels b,c,e, and f. Colors corresponding to locations in panel (a) are plotted across the tops of (b) and (e) (note that the profiler stopped collecting data partway through deployment).

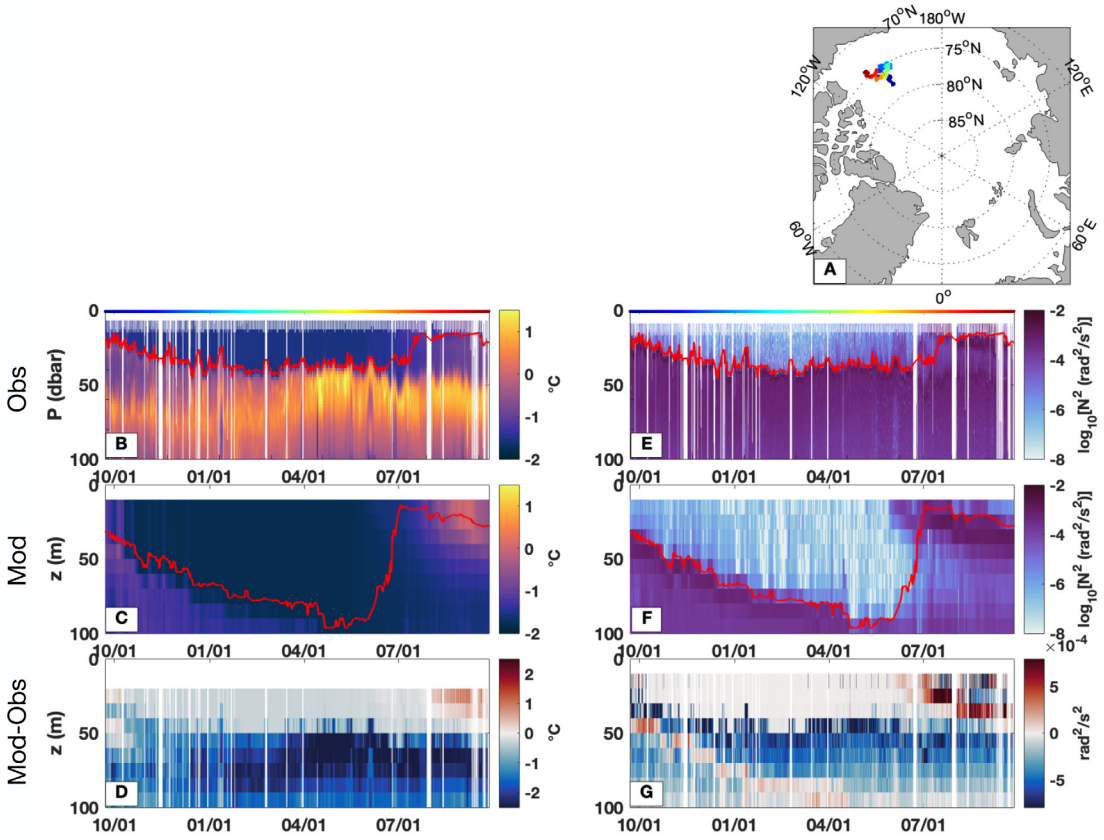

Fig. 15. ITP #114 section in the western Arctic (as in Fig. 14). (a) Overhead map of ITP deployment, (b) observed temperature (°C), (c) modeled temperature along deployment (°C), (d) model-observed temperature difference (°C), (e) observed buoyancy frequency (rad^2 s^{-2}), (f) modeled buoyancy frequency (rad^2 s^{-2}), (g) model-observed buoyancy frequency difference (rad^2 s^{-2}). The mixed layer depth is shown as a red line in panels b,c,e, and f. Colors corresponding to locations in panel (a) are plotted across the tops of (b) and (e).

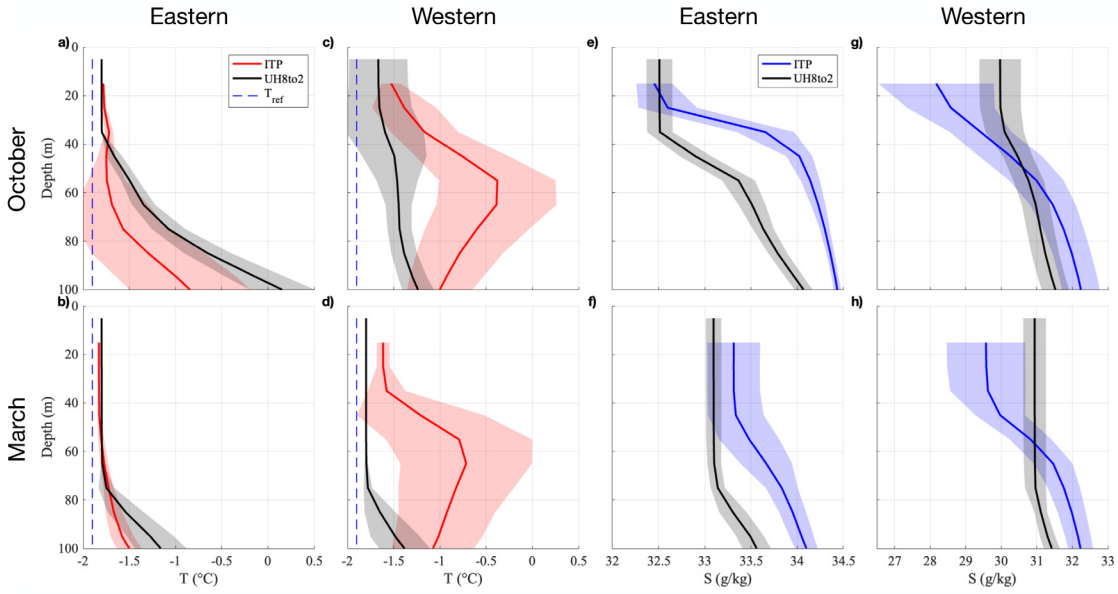

Fig. 16. (a)–(d) Mean temperature (°C) profiles in the upper ocean, for the months of October (a and c) and March (b and d) for the Eastern (a and b) and Western (c and d) Arctic; (e)–(h) Mean salinity (g kg^{-1}) profiles in the upper ocean, for the months of October (e and g) and March (f and h) for the Eastern (e and f) and Western (g and h) Arctic. Colored profiles represent ITP observations, while black profiles are averages from the UH8to2 model. The shaded regions represent two standard deviations around the mean. T_{ref} is the freezing point reference temperature of −1.9 °C.

In the western Arctic, ocean heat content in the upper 100 m is greater in observed profiles than in the UH8to2 simulated counterparts, with the difference being sufficient to melt 70 cm of sea ice per m^2. However, the seasonal evolution of the observed and modeled temperature profiles are very different. In observations, the winter mixed layer stays above 40 m depth in March, allowing the majority of

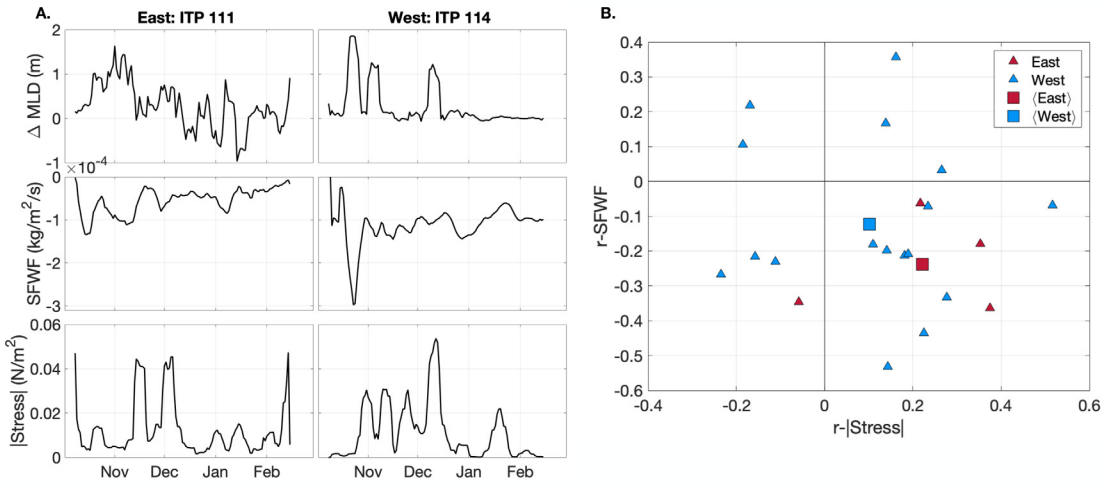

Fig. 17. A. 7-day smoothed time series of the change in mixed layer depth (m; top), net surface freshwater flux (kg m^{-2} s^{-1}; middle), and ice-ocean stress magnitude (N m^{-2}; bottom) in the eastern (left) and western (right) Arctic example ITP deployments. All quantities are for the synthetic UH8to2 ITP deployments. B. Partial correlations (triangles) of the winter change in mixed layer depth with net surface freshwater flux and ice-ocean stress magnitude for each synthetic ITP deployment that had at least 20 profiles between October and March of the following year. Partial correlations are calculated from the 7-day smoothed time series. Mean partial correlations for the eastern and western Arctic are shown as squares.

heat associated with the Pacific Summer Water temperature maximum to remain insulated from the ocean surface. In contrast, the model mixed layer reaches nearly 80 m of depth in March. Comparing the difference in heat content in the upper ocean in both the model and observations from March to October, we find that the change in heat content over this time period is approximately equal in both the model and observations, with both temperature profiles losing enough heat to melt 31 cm of ice per m^2. Thus, while the upper-ocean dynamics are very different between the model and observations, the impact on ice ocean fluxes is apparently identical. For reference, the average integrated UH8to2 bottom melt rate from November through February is 3.4 cm in the western Arctic and 25 cm in the east. Not all available heat melts ice, as some may be used to warm ice to the freezing temperature, lost to the atmosphere, or advected laterally.

In both the eastern and western Arctic, UH8to2 winter mixed layers tend to deepen more than in synoptic observations (Fig. 16). To understand the mechanism driving this deepening, we consider two potential factors across all ITP deployments: the net surface freshwater flux and the ice-ocean stress (scaled here by the ice concentration). In the winter, brine rejection leads to a saltier surface layer across the Arctic, leading to negative freshwater flux (Hunke et al., 2015). This increased salinity results in increased density of the surface mixed layer, potentially leading to convection that causes the mixed layer to deepen. Wind forcing may also deepen the winter mixed layer. In the ice-covered ocean, storms result in inertial oscillations within the sea ice (Brenner et al., 2021; Cole et al., 2018). The 20 min coupling of the ice, ocean, and atmospheric fields in the UH8to2 allows realistic inertial oscillations to develop (Roberts et al., 2015). As the ocean mixed layer responds to the stress induced by the sea ice, shear at the base of the mixed layer increases. This shear can lead to instabilities, and ultimately cause deepening of the mixed layer.

Given these physical mechanisms, we expect the wintertime increase in the mixed layer depth to be negatively correlated with the modeled net surface freshwater flux and positively correlated with the magnitude of modeled ice-ocean stress. We explore these hypotheses by calculating partial-correlation coefficients for both surface freshwater flux and wind stress for each UH8to2-simulated winter ITP deployment. Fig. 17a shows how the mixed layer depth and each of these controlling factors vary over the two modeled example ITP deployments (ITP #111 and #114) discussed in Section 4.1. There are 17 modeled ITP deployments in the western Arctic and 4 in the eastern Arctic which have at least 20 profiles between October and March of the following year. For each of these deployments we calculate partial correlation coefficients for the change in mixed layer depth with the net surface freshwater flux (controlling for the effect of ice-ocean stress magnitude), and between the change in mixed layer depth and ice-ocean stress magnitude (controlling for the effect of net surface freshwater flux; Fig. 17b). All terms are smoothed over a 7-day interval. In the western Arctic, the mean partial correlation coefficient between the change in mixed layer depth and the surface freshwater flux is −0.12 (95% CI: −0.23 to −0.01 across all 17 deployments). The strength of the partial correlation between the change in mixed layer depth and ice-ocean stress magnitude (controlling for the effect of net surface freshwater flux) is comparable, with a mean value of 0.1 (95% CI: 0.004 to 0.20). In the eastern Arctic, the lack of data makes statistical analysis challenging, however calculated values suggest generally similar correlations to those seen in the western Arctic. These results suggest that both brine rejection and ice-ocean stress contribute to mixed layer deepening in both the eastern and western deployments, although neither process accounts for the majority of the variability in mixed layer depth.

5. Discussion

In reviewing the results of the present study, we consider three main angles. First, we discuss the issue of climate feedbacks, their representation in the UH8to2 model, and the climate impacts of model biases. Secondly, we consider these results in the context of other Arctic modeling studies. Finally we discuss areas for future research.

5.1. Climate feedbacks and impacts

In the UH8to2 model, a bias towards low sea ice conditions can be partially explained with reference to ocean biases in the eastern Arctic. Both the brine rejection feedback and the wind–ice–ocean feedback would lead to similar effects that are consistent with the UH8to2 model. These effects include overly deep winter mixed layers and overly weak upper-ocean stratification. Both effects occur throughout the UH8to2 Arctic. However, in the western Arctic, upper-ocean biases in stratification are not associated with significant discrepancies in the heat content available to melt ice, due to offsetting errors between a deeper model winter mixed layer and less model heat storage above 80 m depth. Thus in this region, a full positive feedback loop does not apply, since deeper model mixed layers do not result in meaningfully-increased ocean–ice

heat fluxes. Even though upper-ocean biases in temperature, salinity, and stratification exist in the western Arctic, these biases are not a likely cause of the reduced model ice observed in the western Arctic. We cannot rule out the possibility that atmospheric biases contribute to sea ice biases as well. However, as the JRA55-do atmospheric forcing is a data-assimilative product we think the atmospheric forcing is less likely to lead to errors in sea ice or positive feedback than biases in the ocean model (Tsujino et al., 2018).

We find that both surface freshwater flux and ice-ocean stress are weakly correlated with changes in winter mixed layer depths, suggesting that both brine rejection and shear instability contribute to mixed layer deepening in the model. Both a brine-rejection feedback and a wind–ice–ocean feedback thus have the potential to be active in the UH8to2 simulation. However, overly deep mixed layers may also be caused by initial conditions with insufficient stratification, or due to difficulty in representing Arctic stratification with limited vertical levels. Arctic summer mixed layers are frequently less than 10 m deep (Peralta-Ferriz and Woodgate, 2015), so that realistic representation of both the deepening of mixed layers in the fall and early winter, and the strong stratification at the base of these mixed layers, is very limited given that the UH8to2 vertical grid has a minimum cell height of 10 m. Even the 5 m grid used by Jin et al. (2018) may not be sufficient to fully resolve the mixed layer; cell height of 2 m or less is likely needed to accurately represent this stratification. These potential sources of errors are additional explanations for the overly deep UH8to2 winter mixed layers, and associated elevated vertical heat fluxes, that do not invoke a feedback mechanism. Once the model is in a state with relatively weak stratification, the barrier to deepening winter mixed layers is reduced, so that forcing the model with appropriate surface fluxes will be insufficient to create a realistic upper-ocean seasonal stratification profile. The advection and diffusion terms necessary to close a full mixed layer heat budget (Delman et al., 2018) were not saved in the current model run. Quantifying the contribution of each heat budget term to the mixed layer evolution could be a subject for future study.

Throughout this analysis, we have focused on the effect these mixed layer biases have on ice-ocean heat exchanges. However, the overly deep winter mixed layers have other implications as well. Observational studies indicate warm Pacific Water enters the Beaufort Sea via Barrow Canyon, the Beaufort Shelfbreak Jet, and the Chukchi Slope Current, and is transported by eddies and intrusions into the basin (Corlett and Pickart, 2017; Boury et al., 2020; Lin et al., 2021; Fine et al., 2018; MacKinnon et al., 2021; Fine et al., 2022). The UH8to2 circulation has good representations of these boundary currents thanks to its high horizontal resolution (Fig. 4). These currents carry warm water in the simulation (Fig. 9c). This warm water additionally appears as a passive tracer, showing the separation of eddies from the Chukchi Slope Current (Fig. 9c). UH8to2 sections through Barrow Canyon and the Bering Strait also show realistic distributions of heat (not shown). We therefore conclude that the pathways of warm Pacific inflowing water are reasonably well-represented within the UH8to2 simulation. Thus although the lack of a UH8to2 Pacific Summer Water temperature maximum could be attributed to circulation not captured by the model, it is far more likely that the deeper-than-observed winter mixed layer depths in the model result in the loss of this Pacific-origin heat to the atmosphere and sea ice at the ocean's surface, preventing its accumulation over decadal timescales (Timmermans et al., 2018). The lack of the Pacific subsurface temperature maximum has implications for sound speed estimates, lateral temperature variability, and upper-ocean heat content in the UH8to2 simulation. Sufficient stratification at the base of the mixed layer to prevent the development of overly deep winter mixed layers could be sufficient to improve the Pacific Summer Water representation; whether this realistic stratification could be attained solely by increasing vertical resolution is a topic for future study.

Insofar as the Arctic ocean is sensitive to ice-ocean feedbacks, there is the risk that relatively small initial model biases will lead to increasingly large discrepancies between model and observation, limiting predictive capacity. This concern is of particular relevance given that many other biases can occur in the model throughout the year. Much attention has been given to the ice-albedo effect, in which early ice melt leads to increased insolation through the summer months, which warms the ocean's surface, allowing for more ice to melt. Additionally, late freeze-up in the fall leads to less snow accumulation over the winter, which in turn allows for earlier ice melt (Derksen and Brown, 2012), and early sea ice melt leads to increased ocean evaporation (Boisvert et al., 2015). As well as leading to enhanced atmospheric water vapor, evaporation decreases upper-ocean stratification and could result in deeper mixed layers. All of these feedbacks may operate simultaneously, so that in the worst case scenario relatively small biases in winter mixed-layer deepening processes can lead to a worse summer sea ice representation, which then initiates other feedbacks in both the ocean and atmosphere that result in increasing model biases (Cohen et al., 2014).

5.2. Comparisons with other studies

A number of other studies have focused on the fidelity of Arctic ice-ocean models, or of fully-coupled models in the Arctic ocean. The model biases that we see are within the range of those from other ice-ocean Arctic models (Ilicak et al., 2016; Wang et al., 2016b; Hordoir et al., 2022; Wang et al., 2018). These models have seen vast improvement over recent decades, with earlier models unable to reproduce the halocline stratification observed in the Arctic to the extent that the Pacific Summer Water temperature maximum was entirely absent in all 10 of the models used for a Model Intercomparison Project, which had generally very different Arctic representations (Holloway et al., 2007). In the UH8to2 model we find insufficient halocline stratification in the upper Arctic ocean, however this bias is greatly improved relative to the earlier models, possibly due to changes in model ice-ocean Ekman transport (Roberts et al., 2015). Similar biases are found in the fully coupled CESM1 and CESM2 (Rosenblum et al., 2021).

The UH8to2 model is run with ultrahigh resolution, which leads to improved representation of boundary currents and eddies. Recent work has emphasized the advantages of such ultrahigh resolution, including better insight into how eddy energy is distributed throughout the basin (Wang et al., 2020), how Arctic eddies mediate ice-ocean heat fluxes (Manucharyan and Thompson, 2022), and how higher fidelity sea-ice representations demonstrate the importance of leads in mediating ice-ocean feedbacks (Xu et al., 2021; Hutter et al., 2022). Increasing horizontal resolution allows for insight into the eddy processes that set tracer properties and the flow of energy throughout the basin, and the ice-ocean dynamics that regulate heat transport to the surface. Arctic observations are sparse, and high-resolution models are critical for understanding flows in boundary currents and how changing water properties propagate from Arctic gateway sources.

However, in the current study high lateral resolution does not appear to meaningfully improve upper-ocean stratification, or the representation of winter deepening of mixed layers. This is consistent with work by Chassignet et al. (2020), which found that while higher model resolution improves representation of surface currents and internal variability, higher horizontal resolution does not always lead to improved biases in temperature and salinity, which determine stratification. It is possible that even higher horizontal resolution is necessary to accurately model the mixed-layer processes that restratify the upper ocean (summer mixed layer depths of <10 m correspond to a mixed-layer Rossby number of <3 km, and even the ultrahigh resolution model does not resolve these scales). However, there are simpler dynamics related to vertical mixing that may also lead to this discrepancy. The vertical resolution of the model is coarse relative to observed mixed layer depths, and the model uses the K-Profile Parameterization (KPP) (Large et al., 1994) which is not optimized for the Arctic where mixing rates are weaker than in the global ocean (Guthrie et al., 2013). Zhang et al. (2016) find better representation of Pacific Summer

Water in a model with 5 m near-surface vertical resolution. It is possible that increasing vertical resolution alone would result in some model improvement.

Discrepancies in model brine rejection relative to observations are discussed in depth by Nguyen et al. (2009), who suggest a parameterization to account for the tendency of pockets of brine rejected by sea ice to quickly subduct beneath the mixed layer in plumes, which result in much less mixing than that induced by spreading the equivalent amount of salt over the full surface of a model grid cell, which leads to full convection. Jin et al. (2018) describe differences between a high-resolution regional Arctic model with and without an implementation of such a brine rejection parameterization (Jin et al., 2012; Nguyen et al., 2009) and ice "mushy-layer" thermodynamics (Turner et al., 2013). Including these parameterizations resulted in significant improvements in model temperature, salinity, and mixed layer depth throughout the Arctic. While CICE5 already contains "mushy-layer" thermodynamics, incorporating a brine rejection parameterization might reduce the tendency of the UH8to2 model to form overly deep winter mixed layers.

5.3. Areas for future research

As the model biases we observe, particularly in representations of the heat content, stratification, and depth of Atlantic Water and Pacific Summer Water, are similar to those found in other forced ice-ocean models (Wang et al., 2016a; Ilicak et al., 2016; Hordoir et al., 2022; Wang et al., 2018) and fully-coupled global models (Rosenblum et al., 2021), we suggest that our qualitative conclusions likely apply to other Arctic modeling efforts. Higher resolution models, such as the one described in this study, have the potential to better represent inflowing water masses, boundary currents, and the mean-eddy flow exchanges that regulate heat transport into the Arctic; however, higher resolution models do not necessarily improve temperature or salinity biases. A model that has an initially accurate sea ice field coupled with an ocean with significant temperature and salinity biases is at risk of errors in representing the ice-ocean processes that mediate ice growth and melt cycles which compound over time, as seen in the positive feedbacks discussed in this study. Alternatively, model biases may work out so that the ice-ocean processes result in approximately accurate fluxes in spite of discrepancies in the temperature and salinity in the model, as we found in the western Arctic. Both of these scenarios can limit the utility of the model for future climate projections. Positive ice-ocean feedbacks can lead to errors on seasonal or interannual timescales, while the lack of Pacific Summer Water seen in the model may lead to errors on longer interannual or decadal timescales, if the model is unable to represent future vertical heat fluxes from the warm interior water mass. Conversely, the simulated biases in this model provide an opportunity to understand the physical mechanisms at work in the model and can help in interpreting observations which are by necessity sparse in space and time. These biases also do not preclude the model's usefulness for examining many other processes.

Multiple factors likely contribute to these model biases, and there are many possible avenues to improve model representations of the Arctic upper ocean. Understanding the relative importance of the model limits of vertical resolution and model mixing representations in depicting the seasonal cycle of upper-ocean stratification and mixed layer deepening could provide insight into possible modifications to existing models that would improve the representation of these ice-ocean processes. Arctic model metrics are frequently focused on parameters such as gateway fluxes, Atlantic water temperature and depth, and circulation characteristics (Holloway and Proshutinsky, 2007; Wang et al., 2016b; Ilicak et al., 2016; Hordoir et al., 2022); while these are all important, we suggest that summer and winter mixed layer depths and characteristics of the Pacific Summer Water temperature maximum provide essential insight into the drivers of ocean–ice heat flux. Understanding the small-scale processes that regulate winter ocean–ice heat fluxes is an area of ongoing research (Webster et al. 2022, Rabe et al. 2022, Smith et al. 2022, von Albedyll et al. 2022, and many others), and continuing to develop improved representations and parameterizations of these processes so that models accurately simulate these important exchanges will help improve the accuracy of Arctic climate projections going forward.

6. Summary

The main goal of this work was to compare the UH8to2 Arctic ocean and sea ice simulation with contemporaneous observations and climatology, with an eye towards understanding the influence of model biases on ice-ocean interactions. In this comparison, we found that the UH8to2 model provides high-resolution quasi-realistic Arctic circulation, gateway fluxes, water mass distribution, and sea ice, with

- major current pathways that agree with observations and high eddy activity in the ice-free ocean
- gateway fluxes of volume, fresh water, and heat within a standard deviation of observations
- realistic seasonal cycle in sea-ice extent and thickness
- water mass distribution showing general vertical and spatial structure in agreement with climatology.

While the overall assessment shows promise, several model biases exist. These include

- sea ice extent and concentration biased low in the summer and fall, particularly in the eastern Arctic
- sea ice thickness persistently biased low, with the largest biases occurring in the eastern and central Arctic in the late fall
- Atlantic Water is shallow and warm relative to both climatology and ITP observations
- Pacific Summer Water, which appears in climatology and more dramatically in ITP observations, is largely absent in the UH8to2 model.
- Model stratification is weaker than that of observations and climatology.

We suggest that the model biases in sea ice extent, concentration, and thickness are linked to the model biases in stratification and upper-ocean heat content. Overly deep model winter mixed layers are associated with weak model stratification, resulting in the entrainment of heat from an overly warm and shallow Atlantic Water mass, particularly in the eastern Arctic. These linked processes may accelerate each other through positive feedbacks, including both the brine rejection feedback and the ice–wind–ocean feedback mechanism. The model's impressive horizontal resolution does not effectively overcome these discrepancies in upper-ocean dynamics. Increased vertical resolution or more effective mixed layer parameterizations could potentially help to alleviate this issue.

CRediT authorship contribution statement

Elizabeth C. Fine: Conceptualization, Methodology, Investigation, Formal analysis, Visualization, Writing – original draft, Writing – review & editing. **Julie L. McClean:** Conceptualization, Methodology, Software, Investigation, Formal analysis, Writing – original draft, Writing – review & editing, Supervision, Validation, Visualization, Funding acquisition, Project administration. **Detelina P. Ivanova:** Software, Writing – review & editing. **Anthony P. Craig:** Software, Data curation. **Alan J. Wallcraft:** Conceptualization, Methodology, Software, Writing – review & editing, Funding acquisition. **Eric P. Chassignet:** Conceptualization, Methodology, Writing – review & editing, Funding acquisition, Project administration. **Elizabeth C. Hunke:** Methodology, Writing – review & editing.

Declaration of competing interest

The authors declare the following financial interests/personal relationships which may be considered as potential competing interests: Detelina Ivanova reports a relationship with Climformatics Inc. that includes: board membership, employment, and equity or stocks.

Data availability

Observational data is publicly available; model output used for the analysis is available at https://doi.org/10.6075/J0XK8FQH.

Acknowledgments

The study was funded by the Office of Naval Research, United States grant N00014-19-12674 (E. Chassignet and A. Wallcraft) and via a subcontract from FSU, United States to SIO (J. McClean, E.Fine, A. Craig and D. Ivanova), by the US DOE Office of Science/BER grant DE-SC0020073 (J. McClean, E. Fine, and D. Ivanova), and by BER Science Focus Area funding through the HiLAT project (E. Hunke). The UH8to2 simulation used in this study was produced at the U.S. Army Engineer Research and Development Center (ERDC) DoD Supercomputing Resource Center (DSRC) using computing resources from the Department of Defense (DoD) High Performance Computing Modernization Program (HPCMP), particularly two Pathfinder projects awarded to J. McClean. The simulated background sea-ice state used as an initial condition for the model run in this study was taken from the UH8to2 CORE-II forced simulation run on Cori at the National Energy Research Scientific Computing Center (NERSC). The JRA55-do forcing (https://climate.mri-jma.go.jp/pub/ocean/JRA55-do/) was obtained from the National Center for Atmospheric Research (W. Kim and G. Danabasoglu) who reformatted it for ingestion into CESM. The SSM/I satellite data came from NOAA's PolarWatch Data Catalog (https://polarwatch.noaa.gov/catalog/) via the Environmental Research Division Data Access Program (ERRDAP). C. Zender (UCI) provided the NCO script to interpolate the SSM/I data to a regular grid. CryoSat2 data was made available by the Center for Polar Observation & Modelling Data Portal/European Space Agency (http://www.cpom.ucl.ac.uk/csopr/seaice.php). The WOA18 climatology is provided by the National Oceanic and Atmospheric Administration National Centers for Environmental Information (https://www.ncei.noaa.gov/access/world-ocean-atlas-2018/). The ASTE dataset was downloaded from the National Science Foundation Arctic Data Portal (https://arcticdata.io/catalog/portals/ASTE) and processed using the associated Matlab toolbox. Fram Strait data is available from PANGAEA (https://doi.pangaea.de/10.1594/PANGAEA.904565). Ice-Tethered Profiler data were collected and made available by the Ice-Tethered Profiler Program based at the Woods Hole Oceanographic Institution (https://www.whoi.edu/itp). See also https://github.com/WHOI-ITP for an ITP database tool available for both Matlab and Python that allows users to search for ITP profiles in space and time. The model output described in this analysis is available at https://doi.org/10.6075/J0XK8FQH.

The authors wish to acknowledge use of the Ferret program for analysis and graphics in this paper. Ferret is a product of NOAA's Pacific Marine Environmental Laboratory.

We are grateful to Mathew Maltrud (LANL) for his help in creating the POP ultrahigh model setup, and to all the scientists and technicians involved in the development, deployment, and processing necessary to collect satellite and ITP observations, and in producing the ocean models and climatologies used in this analysis. We are additionally grateful to Dmitry Dukhovskoy, Liz Douglass, Bob Helber, Alexandra Bozec, Patrick Hogan, Xiaobiao Xu, Sarah Gille, Theresa Morrison, Ian Eisenman, Frank Bryan, John Toole, Wilken-Jon von Appen, Wieslaw Maslowski, Marion Alberty, Mary-Louise Timmermans and Mike Steele for scientific support and insight. We also thank our two anonymous reviewers, whose thoughtful comments improved this manuscript.

References

Aksenov, Y., Karcher, M., Proshutinsky, A., Gerdes, R., de Cuevas, B., Golubeva, E., Kauker, F., Nguyen, A.T., Platov, G.A., Wadley, M., Watanabe, E., Coward, A.C., Nurser, A.J.G., 2016. Arctic pathways of Pacific water: Arctic ocean model intercomparison experiments. J. Geophys. Res.: Oceans 121 (1), 27–59. http://dx.doi.org/10.1002/2015JC011299.

Armitage, T.W.K., Bacon, S., Ridout, A.L., Petty, A.A., Wolbach, S., Tsamados, M., 2017. Arctic ocean surface geostrophic circulation 2003–2014. Cryosphere 11 (4), 1767–1780. http://dx.doi.org/10.5194/tc-11-1767-2017.

Bamber, J.L., Tedstone, A.J., King, M.D., Howat, I.M., Enderlin, E.M., van den Broeke, M.R., Noel, B., 2018. Land ice freshwater budget of the Arctic and North Atlantic Oceans: 1. data, methods, and results. J. Geophys. Res.: Oceans 123 (3), 1827–1837. http://dx.doi.org/10.1002/2017JC013605.

Bleck, R., 2002. An oceanic general circulation model framed in hybrid isopycnic-Cartesian coordinates. Ocean Model. 4 (1), 55–88. http://dx.doi.org/10.1016/S1463-5003(01)00012-9.

Boisvert, L.N., Wu, D.L., Shie, C.-L., 2015. Increasing evaporation amounts seen in the Arctic between 2003 and 2013 from AIRS data. J. Geophys. Res.: Atmos. 120 (14), 6865–6881. http://dx.doi.org/10.1002/2015JD023258, URL: http://doi.wiley.com/10.1002/2015JD023258.

Boury, S., Pickart, R.S., Odier, P., Lin, P., Li, M., Fine, E.C., Simmons, H.L., Mackinnon, J.A., Peacock, T., 2020. Whither the Chukchi slope current? J. Phys. Oceanogr. 50 (6), 1717–1732. http://dx.doi.org/10.1175/JPO-D-19-0273.1.

Boyer, T.P., Garcia, H.E., Locarnini, R.A., Zweng, M.M., Mishonov, A.V., Reagan, J.R., Weathers, K.A., Baranova, O.K., Seidov, D., Smolyar, I.V., 2018. World Ocean Atlas 2018. NOAA National Centers for Environmental Information, URL: https://www.ncei.noaa.gov/products/world-ocean-atlas.

Brenner, S., Rainville, L., Thomson, J., Cole, S., Lee, C., 2021. Comparing observations and parameterizations of ice-ocean drag through an annual cycle across the beaufort sea. J. Geophys. Res.: Oceans 126 (4), http://dx.doi.org/10.1029/2020JC016977.

Briegleb, B.P., Light, B., 2007. A delta-eddington multiple scattering parameterization for solar radiation in the sea ice component of the community climate system model (No. NCAR/TN-472+STR). p. 100, University Corporation for Atmospheric Research, DOI: 10.5065/D6B27S71.

Carmack, E., Polyakov, I., Padman, L., Fer, I., Hunke, E., Hutchings, J., Jackson, J., Kelley, D., Kwok, R., Layton, C., Melling, H., Perovich, D., Persson, O., Ruddick, B., Timmermans, M.L., Toole, J., Ross, T., Vavrus, S., Winsor, P., 2015. Toward quantifying the increasing role of oceanic heat in sea ice loss in the new Arctic. Bull. Am. Meteorol. Soc. 96 (12), 2079–2105. http://dx.doi.org/10.1175/BAMS-D-13-00177.1.

Center for Polar Observation and Modelling Data Portal, 2023. Cryosat science background. http://www.cpom.ucl.ac.uk/csopr/science.html.

Chassignet, E.P., Hurlburt, H.E., Metzger, J.E., Smedstad, O.M., Cummings, J.A., Halliwell, G.R., Bleck, R., Baraille, R., Wallcraft, A.J., Lozano, C., Tolman, H.L., Srinivasan, A., Hankin, S., Cornillon, P., Weisberg, R., Barth, A., He, R., Werner, F., Wilkin, J., 2009. US GODAE: Global ocean prediction with the HYbrid Coordinate Ocean Model (HYCOM). Oceanography 22 (2), 64–75, URL: http://www.jstor.org/stable/24860960.

Chassignet, E.P., Smith, L.T., Halliwell, G.R., Bleck, R., 2003. North Atlantic simulations with the Hybrid Coordinate Ocean Model (HYCOM): Impact of the vertical coordinate choice, reference pressure, and thermobaricity. J. Phys. Oceanogr. 33 (12), 2504–2526. http://dx.doi.org/10.1175/1520-0485(2003)033<2504:NASWTH>2.0.CO;2.

Chassignet, E.P., Yeager, S.G., Fox-Kemper, B., Bozec, A., Castruccio, F., Danabasoglu, G., Horvat, C., Kim, W.M., Koldunov, N., Li, Y., Lin, P., Liu, H., Sein, D.V., Sidorenko, D., Wang, Q., Xu, X., 2020. Impact of horizontal resolution on global ocean-sea ice model simulations based on the experimental protocols of the Ocean Model Intercomparison Project phase 2 (OMIP-2). Geosci. Model Dev. 13 (9), 4595–4637. http://dx.doi.org/10.5194/gmd-13-4595-2020.

Cohen, J., Screen, J.A., Furtado, J.C., Barlow, M., Whittleston, D., Coumou, D., Francis, J., Dethloff, K., Entekhabi, D., Overland, J., Jones, J., 2014. Recent Arctic amplification and extreme mid-latitude weather. Nat. Geosci. 7 (9), 627–637. http://dx.doi.org/10.1038/ngeo2234.

Cole, S.T., Stadler, J., 2019. Deepening of the winter mixed layer in the Canada basin, Arctic ocean over 2006–2017. J. Geophys. Res.: Oceans 124 (7), 4618–4630. http://dx.doi.org/10.1029/2019JC014940.

Cole, S.T., Toole, J.M., Rainville, L., Lee, C.M., 2018. Internal waves in the Arctic : Influence of ice concentration , ice roughness , and surface layer strati Fi cation. J. Geophys. Res.: Oceans 123 (8), 5571–5586. http://dx.doi.org/10.1029/2018JC014096.

Comiso, J.C., 2017. Bootstrap sea ice concentrations from nimbus-7 SMMR and DMSP SSM/I-SSMIS, version 3. http://dx.doi.org/10.5067/7Q8HCCWS4I0R, NASA National Snow and Ice Data Center Distributed Active Archive Center, Boulder, Colorado USA.

Corlett, W.B., Pickart, R.S., 2017. The Chukchi slope current. Prog. Oceanogr. 153, 50–65. http://dx.doi.org/10.1016/j.pocean.2017.04.005.

Craig, A.P., Vertenstein, M., Jacob, R., 2012. A new flexible coupler for earth system modeling developed for CCSM4 and CESM1. Int. J. High Perform. Comput. Appl. 26 (1), 31–42. http://dx.doi.org/10.1177/1094342011428141.

Curry, B., Lee, C.M., Petrie, B., Moritz, R.E., Kwok, R., 2014. Multiyear volume, liquid freshwater, and sea ice transports through Davis Strait, 2004-10. J. Phys. Oceanogr. 44 (4), 1244–1266. http://dx.doi.org/10.1175/JPO-D-13-0177.1.

Danabasoglu, G., Yeager, S.G., Bailey, D., Behrens, E., Bentsen, M., Bi, D., Biastoch, A., Böning, C., Bozec, A., Canuto, V.M., Cassou, C., Chassignet, E., Coward, A.C., Danilov, S., Diansky, N., Drange, H., Farneti, R., Fernandez, E., Fogli, P.G., Forget, G., Fujii, Y., Griffies, S.M., Gusev, A., Heimbach, P., Howard, A., Jung, T., Kelley, M., Large, W.G., Leboissetier, A., Lu, J., Madec, G., Marsland, S.J., Masina, S., Navarra, A., George Nurser, A.J., Pirani, A., y Mélia, D.S., Samuels, B.L., Scheinert, M., Sidorenko, D., Treguier, A.M., Tsujino, H., Uotila, P., Valcke, S., Voldoire, A., Wang, Q., 2014. North Atlantic simulations in coordinated ocean-ice reference experiments phase II (CORE-II). Part I: Mean states. Ocean Model. 73, 76–107. http://dx.doi.org/10.1016/j.ocemod.2013.10.005.

de Steur, L., Peralta-Ferriz, C., Pavlova, O., 2018. Freshwater export in the east greenland current freshens the north Atlantic. Geophys. Res. Lett. 45 (24), 13,359–13,366. http://dx.doi.org/10.1029/2018GL080207.

Delman, A.S., McClean, J.L., Sprintall, J., Talley, L.D., Bryan, F.O., 2018. Process-specific contributions to anomalous Java mixed layer cooling during positive IOD events. J. Geophys. Res.: Oceans 123 (6), 4153–4176. http://dx.doi.org/10.1029/2017JC013749.

Depoorter, M.A., Bamber, J.L., Griggs, J.A., Lenaerts, J.T., Ligtenberg, S.R., Van Den Broeke, M.R., Moholdt, G., 2013. Calving fluxes and basal melt rates of Antarctic ice shelves. Nature 502 (7469), 89–92. http://dx.doi.org/10.1038/nature12567.

Derksen, C., Brown, R., 2012. Spring snow cover extent reductions in the 2008–2012 period exceeding climate model projections. Geophys. Res. Lett. 39 (19), 1–6. http://dx.doi.org/10.1029/2012GL053387.

Dukowicz, J.K., Smith, R.D., 1994. Implicit free-surface method for the Bryan-Cox-Semtner ocean model. J. Geophys. Res. 99 (C4), 7991–8014. http://dx.doi.org/10.1029/93JC03455.

Fine, E.C., MacKinnon, J.A., Alford, M.H., Mickett, J.B., 2018. Microstructure observations of turbulent heat fluxes in a warm-core Canada basin eddy. J. Phys. Oceanogr. 48 (10), 2397–2418. http://dx.doi.org/10.1175/JPO-D-18-0028.1, URL: https://journals.ametsoc.org/view/journals/phoc/48/10/jpo-d-18-0028.1.xml.

Fine, E.C., MacKinnon, J.A., Alford, M.H., Middleton, L., Taylor, J., Mickett, J.B., Cole, S.T., Couto, N., Boyer, A.L., Peacock, T., 2022. Double diffusion, shear instabilities, and heat impacts of a Pacific summer water intrusion in the Beaufort sea. J. Phys. Oceanogr. 52 (2), 189–203. http://dx.doi.org/10.1175/JPO-D-21-0074.1, URL: https://journals.ametsoc.org/view/journals/phoc/52/2/JPO-D-21-0074.1.xml.

Giles, K.A., Laxon, S.W., Wingham, D.J., Wallis, D.W., Krabill, W.B., Leuschen, C.J., McAdoo, D., Manizade, S.S., Raney, R.K., 2007. Combined airborne laser and radar altimeter measurements over the Fram Strait in May 2002. Remote Sens. Environ. 111 (2), 182–194. http://dx.doi.org/10.1016/j.rse.2007.02.037.

Guthrie, J.D., Morison, J.H., Fer, I., 2013. Revisiting internal waves and mixing in the Arctic ocean. J. Geophys. Res.: Oceans 118 (8), 3966–3977. http://dx.doi.org/10.1002/jgrc.20294.

Hecht, M., Veneziani, M., Weijer, W., Kravitz, B., Burrows, S., Comeau, D., Hunke, E., Jeffery, N., Urrego-Blanco, J., Wang, H., Wang, S., Zhang, J., Bailey, D., Mills, C., Rasch, P., Urban, N., 2019. E3SMv0-HiLAT: A modified climate system model targeted for the study of high-latitude processes. J. Adv. Modelling Earth Syst. 11 (8), 2814–2843. http://dx.doi.org/10.1029/2018MS001524.

Holloway, G., Dupont, F., Golubeva, E., Häkkinen, S., Hunke, E., Jin, M., Karcher, M., Kauker, F., Maltrud, M., Morales Maqueda, M.A., Maslowski, W., Platov, G., Stark, D., Steele, M., Suzuki, T., Wang, J., Zhang, J., 2007. Water properties and circulation in Arctic ocean models. J. Geophys. Res.: Oceans 112 (4), 1–18. http://dx.doi.org/10.1029/2006JC003642.

Holloway, G., Proshutinsky, A., 2007. Role of tides in Arctic ocean/ice climate. J. Geophys. Res.: Oceans 112 (4), http://dx.doi.org/10.1029/2006JC003643.

Hordoir, R., Skagseth, Ø., Ingvaldsen, R.B., Sandø, A.B., Löptien, U., Dietze, H., Gierisch, A.M., Assmann, K.M., Lundesgaard, Ø., Lind, S., 2022. Changes in Arctic stratification and mixed layer depth cycle: A modeling analysis. J. Geophys. Res.: Oceans 127 (1), 1–30. http://dx.doi.org/10.1029/2021JC017270.

Hunke, E.C., Hebert, D.A., Lecomte, O., 2013. Level-ice melt ponds in the Los Alamos sea ice model, CICE. Ocean Model. 71, 26–42. http://dx.doi.org/10.1016/j.ocemod.2012.11.008.

Hunke, E.C., Lipscomb, W.H., Turner, A.K., Jeffery, N., Elliot, S., 2015. CICE : the Los Alamos Sea Ice Model Documentation and Software User's Manual Version 5.1 LA-CC-06-012. Tech. Rep. la-CC-06-012, (March 17), Los Alamos National Laboratory, p. 76.

Hurrell, J.W., Holland, M.M., Gent, P.R., Ghan, S., Kay, J.E., Kushner, P.J., Lamarque, J.F., Large, W.G., Lawrence, D., Lindsay, K., Lipscomb, W.H., Long, M.C., Mahowald, N., Marsh, D.R., Neale, R.B., Rasch, P., Vavrus, S., Vertenstein, M., Bader, D., Collins, W.D., Hack, J.J., Kiehl, J., Marshall, S., 2013. The community earth system model: A framework for collaborative research. Bull. Am. Meteorol. Soc. 94 (9), 1339–1360. http://dx.doi.org/10.1175/BAMS-D-12-00121.1.

Hutter, N., Bouchat, A., Dupont, F., Dukhovskoy, D., Koldunov, N., Lee, Y.J., Lemieux, J.F., Lique, C., Losch, M., Maslowski, W., Myers, P.G., Ólason, E., Rampal, P., Rasmussen, T., Talandier, C., Tremblay, B., Wang, Q., 2022. Sea ice rheology experiment (SIREx): 2. Evaluating linear kinematic features in high-resolution sea ice simulations. J. Geophys. Res.: Oceans 127 (4), http://dx.doi.org/10.1029/2021JC017666.

Ilicak, M., Drange, H., Wang, Q., Gerdes, R., Aksenov, Y., Bailey, D., Bentsen, M., Biastoch, A., Bozec, A., Böning, C., Cassou, C., Chassignet, E., Coward, A.C., Curry, B., Danabasoglu, G., Danilov, S., Fernandez, E., Fogli, P.G., Fujii, Y., Griffies, S.M., Iovino, D., Jahn, A., Jung, T., Large, W.G., Lee, C., Lique, C., Lu, J., Masina, S., George Nurser, A.J., Roth, C., Salas y Mélia, D., Samuels, B.L., Spence, P., Tsujino, H., Valcke, S., Voldoire, A., Wang, X., Yeager, S.G., 2016. An assessment of the Arctic ocean in a suite of interannual CORE-II simulations. Part III: Hydrography and fluxes. Ocean Model. 100, 141–161. http://dx.doi.org/10.1016/j.ocemod.2016.02.004.

Jackson, J.M., Carmack, E.C., McLaughlin, F.A., Allen, S.E., Ingram, R.G., 2010. Identification, characterization, and change of the near-surface temperature maximum in the Canada Basin, 1993–2008. J. Geophys. Res.: Oceans 115 (5), 1–16. http://dx.doi.org/10.1029/2009JC005265.

Jin, M., Deal, C., Maslowski, W., Matrai, P., Roberts, A., Osinski, R., Lee, Y.J., Frants, M., Elliott, S., Jeffery, N., Hunke, E., Wang, S., 2018. Effects of model resolution and ocean mixing on forced ice-ocean physical and biogeochemical simulations using global and regional system models. J. Geophys. Res.: Oceans 123 (1), 358–377. http://dx.doi.org/10.1002/2017JC013365.

Jin, M., Hutchings, J., Kawaguchi, Y., Kikuchi, T., 2012. Ocean mixing with lead-dependent subgrid scale brine rejection parameterization in a climate model. J. Ocean Univ. China 11 (4), 473–480. http://dx.doi.org/10.1007/s11802-012-2094-4.

Krishfield, R., Toole, J., Proshutinsky, A., Timmermans, M.L., 2008. Automated ice-tethered profilers for seawater observations under pack ice in all seasons. J. Atmos. Ocean. Technol. 25 (11), 2091–2105. http://dx.doi.org/10.1175/2008JTECHO587.1.

Kurtz, N., Harbeck, J., 2017. CryoSat-2 Level-4 Sea Ice Elevation, Freeboard, and Thickness, Version 1. NASA National Snow and Ice Data Center Distributed Active Archive Center, Boulder, Colorado USA.

Large, W.G., McWilliams, J.C., Doney, S.C., 1994. Oceanic vertical mixing: A review and a model with a nonlocal boundary layer parameterization. Rev. Geophys. 32 (4), 363–403. http://dx.doi.org/10.1029/94RG01872.

Large, W.G., Yeager, S.G., 2009. The global climatology of an interannually varying air - Sea flux data set. Clim. Dynam. 33 (2–3), 341–364. http://dx.doi.org/10.1007/s00382-008-0441-3.

Lavoie, J., Tremblay, B., Rosenblum, E., 2022. Pacific waters pathways and vertical mixing in the CESM1-LE: Implication for mixed layer depth evolution and sea ice mass balance in the Canada basin. J. Geophys. Res.: Oceans 127 (2), 1–18. http://dx.doi.org/10.1029/2021jc017729.

Laxon, S.W., Giles, K.A., Ridout, A.L., Wingham, D.J., Willatt, R., Cullen, R., Kwok, R., Schweiger, A., Zhang, J., Haas, C., Hendricks, S., Krishfield, R., Kurtz, N., Farrell, S., Davidson, M., 2013. CryoSat-2 estimates of Arctic sea ice thickness and volume. Geophys. Res. Lett. 40 (4), 732–737. http://dx.doi.org/10.1002/grl.50193.

Leng, H., Spall, M.A., Pickart, R.S., Lin, P., Bai, X., 2021. Origin and fate of the Chukchi slope current using a numerical model and in-situ data. J. Geophys. Res.: Oceans 126 (5), 1–19. http://dx.doi.org/10.1029/2021JC017291.

Lin, P., Pickart, R.S., Våge, K., Li, J., 2021. Fate of warm Pacific water in the Arctic basin. Geophys. Res. Lett. 48 (20), 1–12. http://dx.doi.org/10.1029/2021gl094693.

Lindsay, R., Schweiger, A., 2015. Arctic sea ice thickness loss determined using subsurface, aircraft, and satellite observations. Cryosphere 9 (1), 269–283. http://dx.doi.org/10.5194/tc-9-269-2015.

MacKinnon, J.A., Simmons, H.L., Hargrove, J., Thomson, J., Peacock, T., Alford, M.H., Barton, B.I., Boury, S., Brenner, S.D., Couto, N., Danielson, S.L., Fine, E.C., Graber, H.C., Guthrie, J., Hopkins, J.E., Jayne, S.R., Jeon, C., Klenz, T., Lee, C.M., Lenn, Y.D., Lucas, A.J., Lund, B., Mahaffey, C., Norman, L., Rainville, L., Smith, M.M., Thomas, L.N., Torres-Valdés, S., Wood, K.R., 2021. A warm jet in a cold ocean. Nature Commun. 12 (1), 1–12. http://dx.doi.org/10.1038/s41467-021-22505-5.

Maltrud, M.E., McClean, J.L., 2005. An eddy resolving global 1/10 ocean simulation. Ocean Model. 8 (1–2), 31–54. http://dx.doi.org/10.1016/j.ocemod.2003.12.001, URL: https://linkinghub.elsevier.com/retrieve/pii/S1463500303000684.

Manucharyan, G.E., Thompson, A.F., 2022. Heavy footprints of upper-ocean eddies on weakened Arctic sea ice in marginal ice zones. Nature Commun. 13 (1), 1–10. http://dx.doi.org/10.1038/s41467-022-29663-0.

McClean, J.L., Bader, D.C., Bryan, F.O., Maltrud, M.E., Dennis, J.M., Mirin, A.A., Jones, P.W., Kim, Y.Y., Ivanova, D.P., Vertenstein, M., Boyle, J.S., Jacob, R.L., Norton, N., Craig, A., Worley, P.H., 2011. A prototype two-decade fully-coupled fine-resolution CCSM simulation. Ocean Model. 39 (1–2), 10–30. http://dx.doi.org/10.1016/j.ocemod.2011.02.011, https://linkinghub.elsevier.com/retrieve/pii/S1463500311000461.

Metzger, E.J., Hogan, P., Shriver, J.F., Thoppil, P.G., Douglass, E., Yu, Z., Allard, R.A., Rowley, C.D., Phelps, M.W., 2020. Validation test report for the global ocean forecast system 3 . 5 – 1 / 25º HYCOM / CICE with tides. Naval Research Laboratory, p. 70.

Metzger, J.E., Smedstad, O.M., Thoppil, P.G., Hurlburt, H.E., Cummings, J.A., Wallcraft, A.J., Zamudio, L., Franklin, D.S., Posey, P.G., Phelps, M.W., Hogan, P.J., Bub, F.L., DeHaan, C.J., 2014. US navy operational global ocean and Arctic ice prediction systems. Oceanography 27 (3), 32–43. http://dx.doi.org/10.5670/oceanog.2014.66.

Morrison, T.J., 2022. From Greenland Fjords to the Labrador Sea: Mechanisms of Heat and Freshwater Transport in Mesoscale Eddy Active Ocean/Sea-ice Simulations (Ph.D. thesis). University of California San Diego.

Münchow, A., Melling, H., Falkner, K.K., 2006. An observational estimate of volume and freshwater flux leaving the Arctic ocean through nares strait. J. Phys. Oceanogr. 36 (11), 2025–2041. http://dx.doi.org/10.1175/JPO2962.1.

Nguyen, A.T., Menemenlis, D., Kwok, R., 2009. Improved modeling of the Arctic halocline with a subgrid-scale brine rejection parameterization. J. Geophys. Res.: Oceans 114 (11), 1–12. http://dx.doi.org/10.1029/2008JC005121.

Nguyen, A.T., Pillar, H., Ocaña, V., Bigdeli, A., Smith, T.A., Heimbach, P., 2021. The Arctic subpolar gyre state estimate: Description and assessment of a data-constrained, dynamically consistent ocean-sea ice estimate for 2002–2017. J. Adv. Modelling Earth Syst. 13 (5), 1–49. http://dx.doi.org/10.1029/2020MS002398.

Nurser, A.J., Bacon, S., 2014. The Rossby radius in the Arctic ocean. Ocean Sci. 10 (6), 967–975. http://dx.doi.org/10.5194/os-10-967-2014.

Peralta-Ferriz, C., Woodgate, R.A., 2015. Seasonal and interannual variability of pan-arctic surface mixed layer properties from 1979 to 2012 from hydrographic data, and the dominance of stratification for multiyear mixed layer depth shoaling. Prog. Oceanogr. 134, 19–53. http://dx.doi.org/10.1016/j.pocean.2014.12.005.

Perovich, D.K., Richter-Menge, J.A., 2015. Regional variability in sea ice melt in a changing Arctic. Phil. Trans. R. Soc. A 373 (2045), http://dx.doi.org/10.1098/rsta.2014.0165.

Pickart, R.S., Weingartner, T.J., Pratt, L.J., Zimmermann, S., Torres, D.J., 2005. Flow of winter-transformed Pacific water into the western Arctic. Deep-Sea Res. II: Top. Stud. Oceanogr. 52 (24–26), 3175–3198. http://dx.doi.org/10.1016/j.dsr2.2005.10.009.

Polyakov, I.V., Pnyushkov, A.V., Alkire, M.B., Ashik, I.M., Baumann, T.M., Carmack, E.C., Goszczko, I., Guthrie, J., Ivanov, V.V., Kanzow, T., Krishfield, R., Kwok, R., Sundfjord, A., Morison, J., Rember, R., Yulin, A., 2017. Greater role for Atlantic inflows on sea-ice loss in the Eurasian Basin of the Arctic ocean. Science 356 (6335), 285–291. http://dx.doi.org/10.1126/science.aai8204.

Polyakov, I.V., Pnyushkov, A.V., Carmack, E.C., 2018. Stability of the Arctic halocline: A new indicator of Arctic climate change. Environ. Res. Lett. 13 (12), http://dx.doi.org/10.1088/1748-9326/aaec1e.

Polyakov, I.V., Rippeth, T.P., Fer, I., Alkire, M.B., Baumann, T.M., Carmack, E.C., Ingvaldsen, R., Ivanov, V.V., Janout, M., Lind, S., Padman, L., Pnyushkov, A.V., Rember, R., 2020a. Weakening of cold halocline layer exposes sea ice to oceanic heat in the eastern Arctic ocean. J. Clim. 33 (18), 8107–8123. http://dx.doi.org/10.1175/JCLI-D-19-0976.1.

Polyakov, I.V., Rippeth, T.P., Fer, I., Baumann, T.M., Carmack, E.C., Ivanov, V.V., Janout, M., Padman, L., Pnyushkov, A.V., Rember, R., 2020b. Intensification of near-surface currents and shear in the Eastern Arctic ocean. Geophys. Res. Lett. 47 (16), 1–9. http://dx.doi.org/10.1029/2020GL089469.

Pringle, D.J., Eicken, H., Trodahl, H.J., Backstrom, L.G., 2007. Thermal conductivity of landfast Antarctic and Arctic sea ice. J. Geophys. Res.: Oceans 112 (4), 1–13. http://dx.doi.org/10.1029/2006JC003641.

Proshutinsky, A., Krishfield, R., Toole, J.M., Timmermans, M.L., Williams, W., Zimmermann, S., Yamamoto-Kawai, M., Armitage, T.W., Dukhovskoy, D., Golubeva, E., Manucharyan, G.E., Platov, G., Watanabe, E., Kikuchi, T., Nishino, S., Itoh, M., Kang, S.H., Cho, K.H., Tateyama, K., Zhao, J., 2019. Analysis of the beaufort gyre freshwater content in 2003–2018. J. Geophys. Res.: Oceans 124 (12), 9658–9689. http://dx.doi.org/10.1029/2019JC015281.

Rabe, B., Heuzé, C., Regnery, J., Aksenov, Y., Allerholt, J., Athanase, M., Bai, Y., Basque, C., Bauch, D., Baumann, T.M., Chen, D., Cole, S.T., Craw, L., Davies, A., Damm, E., Dethloff, K., Divine, D.V., Doglioni, F., Ebert, F., Fang, Y.C., Fer, I., Fong, A.A., Gradinger, R., Granskog, M.A., Graupner, R., Haas, C., He, H., He, Y., Hoppmann, M., Janout, M., Kadko, D., Kanzow, T., Karam, S., Kawaguchi, Y., Koenig, Z., Kong, B., Krishfield, R.A., Krumpen, T., Kuhlmey, D., Kuznetsov, I., Lan, M., Laukert, G., Lei, R., Li, T., Torres-Valdés, S., Lin, L., Lin, L., Liu, H., Liu, N., Loose, B., Ma, X., McKay, R., Mallet, M., Mallett, R.D., Maslowski, W., Mertens, C., Mohrholz, V., Muilwijk, M., Nicolaus, M., O'Brien, J.K., Perovich, D., Ren, J., Rex, M., Ribeiro, N., Rinke, A., Schaffer, J., Schuffenhauer, I., Schulz, K., Shupe, M.D., Shaw, W., Sokolov, V., Sommerfeld, A., Spreen, G., Stanton, T., Stephens, M., Su, J., Sukhikh, N., Sundfjord, A., Thomisch, K., Tippenhauer, S., Toole, J.M., Vredenborg, M., Walter, M., Wang, H., Wang, L., Wang, Y., Wendisch, M., Zhao, J., Zhou, M., Zhu, J., 2022. Overview of the MOSAiC expedition: Physical oceanography. Elementa, Vol. 10, no. 1. pp. 1–31. http://dx.doi.org/10.1525/elementa.2021.00062.

Rabe, B., Schauer, U., Mackensen, A., Karcher, M., Hansen, E., Beszczynska-Möller, A., 2009. Freshwater components and transports in the Fram Strait – recent observations and changes since the late 1990s. Ocean Sci. 5 (3), 219–233. http://dx.doi.org/10.5194/os-5-219-2009.

Roberts, A., Craig, A., Maslowski, W., Osinski, R., Duvivier, A., Hughes, M., Nijssen, B., Cassano, J., Brunke, M., 2015. Simulating transient ice-ocean ekman transport in the regional Arctic system model and community earth system model. Ann. Glaciol. 56 (69), 211–228. http://dx.doi.org/10.3189/2015AoG69A760.

Rosenblum, E., Fajber, R., Stroeve, J.C., Gille, S.T., Tremblay, L.B., Carmack, E.C., 2021. Surface salinity under transitioning ice cover in the Canada Basin: Climate model biases linked to vertical distribution of fresh water. Geophys. Res. Lett. 48 (21), http://dx.doi.org/10.1029/2021GL094739.

Rothrock, D.A., 1975. The energetics of the plastic deformation of pack ice by ridging. J. Geophys. Res. 80 (33), 4514–4519. http://dx.doi.org/10.1029/JC080i033p04514, URL: http://doi.wiley.com/10.1029/JC080i033p04514.

Rudels, B., Jones, E.P., Schauer, U., Eriksson, P., 2004. Atlantic sources of the Arctic ocean surface and halocline waters. Polar Res. 23 (2), 181–208. http://dx.doi.org/10.3402/polar.v23i2.6278.

Schauer, U., Fahrbach, E., Osterhus, S., Rohardt, G., 2004. Arctic warming through the fram strait: Oceanic heat transport from 3 years of measurements. J. Geophys. Res. C: Oceans 109 (6), 1–14. http://dx.doi.org/10.1029/2003JC001823.

Segtnan, O.H., Furevik, T., Jenkins, A.D., 2011. Heat and freshwater budgets of the nordic seas computed from atmospheric reanalysis and ocean observations. J. Geophys. Res.: Oceans 116 (11), 1–17. http://dx.doi.org/10.1029/2011JC006939.

Shimada, K., Carmack, E.C., Hatakeyama, K., Takizawa, T., 2001. Varieties of shallow temperature maximum waters in the Western Canadian Basin of the Arctic ocean. Geophys. Res. Lett. 28 (18), 3441–3444. http://dx.doi.org/10.1029/2001GL013168.

Smedsrud, L.H., Esau, I., Ingvaldsen, R.B., Eldevik, T., Haugan, P.M., Li, C., Lien, V.S., Olsen, A., Omar, A.M., Risebrobakken, B., Sandø, A.B., Semenov, V.A., Sorokina, S.A., 2013. The role of the barents sea in the Arctic climate system. Rev. Geophys. 51 (3), 415–449. http://dx.doi.org/10.1002/rog.20017.

Smith, M.M., von Albedyll, L., Raphael, I.A., Lange, B.A., Matero, I., Salganik, E., Webster, M.A., Granskog, M.A., Fong, A., Lei, R., Light, B., 2022. Quantifying false bottoms and under-ice meltwater layers beneath Arctic summer sea ice with fine-scale observations. Elementa: Sci. Anthropocene 10 (1), 1–19. http://dx.doi.org/10.1525/elementa.2021.000116.

Steele, M., Morison, J., Ermold, W., Rigor, I., Ortmeyer, M., Shimada, K., 2004. Circulation of summer Pacific halocline water in the Arctic ocean. J. Geophys. Res.: Oceans 109 (2), 1–18. http://dx.doi.org/10.1029/2003jc002009.

Steele, M., Morley, R., Ermold, W., 2001. PHC: A global ocean hydrography with a high-quality Arctic ocean. J. Clim. 14 (9), 2079–2087. http://dx.doi.org/10.1175/1520-0442(2001)014<2079:PAGOHW>2.0.CO;2.

Stroeve, J., Notz, D., 2018. Changing state of Arctic sea ice across all seasons. Environ. Res. Lett. 13 (10), http://dx.doi.org/10.1088/1748-9326/aade56.

Stroeve, J.C., Serreze, M.C., Holland, M.M., Kay, J.E., Malanik, J., Barrett, A.P., 2012. The Arctic's rapidly shrinking sea ice cover: A research synthesis. Clim. Change 110 (3–4), 1005–1027. http://dx.doi.org/10.1007/s10584-011-0101-1.

Timmermans, M.-L., Proshutinsky, A., Golubeva, E., Jackson, J.M., Krishfield, R., McCall, M., Platov, G., Toole, J., Williams, W., Kikuchi, T., Nishino, S., 2014. Mechanisms of Pacific summer water variability in the Arctic's central Canada basin. J. Geophys. Res.: Oceans 119 (11), 7523–7548. http://dx.doi.org/10.1002/2014JC010273.

Timmermans, M.L., Toole, J., Krishfield, R., 2018. Warming of the interior Arctic ocean linked to sea ice losses at the basin margins. Sci. Adv. 4 (8), 1–7. http://dx.doi.org/10.1126/sciadv.aat6773.

Toole, J.M., Timmermans, M.L., Perovich, D.K., Krishfield, R.A., Proshutinsky, A., Richter-Menge, J.A., 2010. Influences of the ocean surface mixed layer and thermohaline stratification on Arctic sea ice in the central Canada Basin. J. Geophys. Res.: Oceans 115 (10), 1–14. http://dx.doi.org/10.1029/2009JC005660.

Tsamados, M., Feltham, D.L., Wilchinsky, A.V., 2013. Impact of a new anisotropic rheology on simulations of Arctic Sea ice. J. Geophys. Res.: Oceans 118 (1), 91–107. http://dx.doi.org/10.1029/2012JC007990.

Tsujino, H., Urakawa, S., Nakano, H., Small, R.J., Kim, W.M., Yeager, S.G., Danabasoglu, G., Suzuki, T., Bamber, J.L., Bentsen, M., Böning, C.W., Bozec, A., Chassignet, E.P., Curchitser, E., Boeira Dias, F., Durack, P.J., Griffies, S.M., Harada, Y., Ilicak, M., Josey, S.A., Kobayashi, C., Kobayashi, S., Komuro, Y., Large, W.G., Le Sommer, J., Marsland, S.J., Masina, S., Scheinert, M., Tomita, H., Valdivieso, M., Yamazaki, D., 2018. JRA-55 based surface dataset for driving ocean–sea-ice models (JRA55-do). Ocean Model. 130 (July), 79–139. http://dx.doi.org/10.1016/j.ocemod.2018.07.002.

Turner, A.K., Hunke, E.C., Bitz, C.M., 2013. Two modes of sea-ice gravity drainage: A parameterization for large-scale modeling. J. Geophys. Res.: Oceans 118 (5), 2279–2294. http://dx.doi.org/10.1002/jgrc.20171.

Uotila, P., Goosse, H., Haines, K., Chevallier, M., Barthélemy, A., Bricaud, C., Carton, J., Fučkar, N., Garric, G., Iovino, D., Kauker, F., Korhonen, M., Lien, V.S., Marnela, M., Massonnet, F., Mignac, D., Peterson, K.A., Sadikni, R., Shi, L., Tietsche, S., Toyoda, T., Xie, J., Zhang, Z., 2019. An assessment of ten ocean reanalyses in the polar regions. Climate Dynamics, Vol. 52, no. 3–4. Springer Berlin Heidelberg, pp. 1613–1650. http://dx.doi.org/10.1007/s00382-018-4242-z.

Våge, K., Pickart, R.S., Spall, M.A., Moore, G.W., Valdimarsson, H., Torres, D.J., Erofeeva, S.Y., Nilsen, J.E.Ø., 2013. Revised circulation scheme north of the Denmark strait. Deep-Sea Res. I: Oceanogr. Res. Pap. 79, 20–39. http://dx.doi.org/10.1016/j.dsr.2013.05.007.

von Albedyll, L., Hendricks, S., Grodofzig, R., Krumpen, T., Arndt, S., Belter, H.J., Birnbaum, G., Cheng, B., Hoppmann, M., Hutchings, J., Itkin, P., Lei, R., Nicolaus, M., Ricker, R., Rohde, J., Suhrhoff, M., Timofeeva, A., Watkins, D., Webster, M., Haas, C., 2022. Thermodynamic and dynamic contributions to seasonal Arctic sea ice thickness distributions from airborne observations. Elementa 10 (1), 1–27. http://dx.doi.org/10.1525/elementa.2021.00074.

von Appen, W.-J., 2019. Physical oceanography and current meter data (including raw data) from FRAM moorings in the fram strait, 2016–2018. PANGAEA, http://dx.doi.org/10.1594/PANGAEA.904565.

von Appen, W.-J., Beszczynska-Möller, A., Schauer, U., Fahrbach, E., 2019. Physical oceanography and current meter data from moorings F1-F14 and F15/F16 in the fram strait, 1997–2016. PANGAEA, http://dx.doi.org/10.1594/PANGAEA.900883.

Wang, Q., Ilicak, M., Gerdes, R., Drange, H., Aksenov, Y., Bailey, D.A., Bentsen, M., Biastoch, A., Bozec, A., Böning, C., Cassou, C., Chassignet, E., Coward, A.C., Curry, B., Danabasoglu, G., Danilov, S., Fernandez, E., Fogli, P.G., Fujii, Y., Griffies, S.M., Iovino, D., Jahn, A., Jung, T., Large, W.G., Lee, C., Lique, C., Lu, J., Masina, S., Nurser, A.J., Rabe, B., Roth, C., Salas y Mélia, D., Samuels, B.L., Spence, P., Tsujino, H., Valcke, S., Voldoire, A., Wang, X., Yeager, S.G., 2016a. An assessment of the Arctic ocean in a suite of interannual CORE-II simulations. Part I: Sea ice and solid freshwater. Ocean Model. 99, 110–132. http://dx.doi.org/10.1016/j.ocemod.2015.12.008.

Wang, Q., Ilicak, M., Gerdes, R., Drange, H., Aksenov, Y., Bailey, D.A., Bentsen, M., Biastoch, A., Bozec, A., Böning, C., Cassou, C., Chassignet, E., Coward, A.C., Curry, B., Danabasoglu, G., Danilov, S., Fernandez, E., Fogli, P.G., Fujii, Y., Griffies, S.M., Iovino, D., Jahn, A., Jung, T., Large, W.G., Lee, C., Lique, C., Lu, J., Masina, S., Nurser, A.J., Rabe, B., Roth, C., Salas y Mélia, D., Samuels, B.L., Spence, P., Tsujino, H., Valcke, S., Voldoire, A., Wang, X., Yeager, S.G., 2016b. An assessment of the Arctic ocean in a suite of interannual CORE-II simulations. Part II: Liquid freshwater. Ocean Model. 99, 86–109. http://dx.doi.org/10.1016/j.ocemod.2015.12.009.

Wang, Q., Koldunov, N.V., Danilov, S., Sidorenko, D., Wekerle, C., Scholz, P., Bashmachnikov, I.L., Jung, T., 2020. Eddy kinetic energy in the Arctic ocean from a global simulation with a 1-km Arctic. Geophys. Res. Lett. 47 (14), http://dx.doi.org/10.1029/2020GL088550.

Wang, Q., Wekerle, C., Danilov, S., Wang, X., Jung, T., 2018. A 4.5g km resolution Arctic ocean simulation with the global multi-resolution model FESOM 1.4. Geosci. Model Dev. 11 (4), 1229–1255. http://dx.doi.org/10.5194/gmd-11-1229-2018.

Weatherall, P., Marks, K.M., Jakobsson, M., Schmitt, T., Tani, S., Arndt, J.E., Rovere, M., Chayes, D., Ferrini, V., Wigley, R., 2015. A new digital bathymetric model of the world's oceans. Earth Space Sci. 2 (8), 331–345. http://dx.doi.org/10.1002/2015EA000107.

Webster, M.A., Holland, M., Wright, N.C., Hendricks, S., Hutter, N., Itkin, P., Light, B., Linhardt, F., Perovich, D.K., Raphael, I.A., Smith, M.M., Von Albedyll, L., Zhang, J., 2022. Spatiotemporal evolution of melt ponds on Arctic sea ice: MOSAiC observations and model results. Elementa 10 (1), 1–22. http://dx.doi.org/10.1525/elementa.2021.000072.

Wekerle, C., Wang, Q., von Appen, W.J., Danilov, S., Schourup-Kristensen, V., Jung, T., 2017. Eddy-resolving simulation of the Atlantic water circulation in the fram strait with focus on the seasonal cycle. J. Geophys. Res.: Oceans 122 (11), 8385–8405. http://dx.doi.org/10.1002/2017JC012974.

Woodgate, R.A., 2018. Increases in the Pacific inflow to the Arctic from 1990 to 2015, and insights into seasonal trends and driving mechanisms from year-round bering strait mooring data. Prog. Oceanogr. 160, 124–154. http://dx.doi.org/10.1016/j.pocean.2017.12.007.

Woodgate, R.A., Weingartner, T.J., Lindsay, R., 2012. Observed increases in Bering strait oceanic fluxes from the Pacific to the Arctic from 2001 to 2011 and their impacts on the Arctic ocean water column. Geophys. Res. Lett. 39 (24), 2–7. http://dx.doi.org/10.1029/2012GL054092.

Xu, S., Ma, J., Zhou, L., Zhang, Y., Liu, J., Wang, B., 2021. Comparison of sea ice kinematics at different resolutions modeled with a grid hierarchy in the Community Earth System Model (version 1.2.1). Geosci. Model Dev. 14 (1), 603–628. http://dx.doi.org/10.5194/gmd-14-603-2021.

Yeager, S., Karspeck, A., Danabasoglu, G., Tribbia, J., Teng, H., 2012. A decadal prediction case study: Late twentieth-century north Atlantic Ocean heat content. J. Clim. 25 (15), 5173–5189. http://dx.doi.org/10.1175/JCLI-D-11-00595.1.

Zhang, J., Steele, M., Runciman, K., Dewey, S., Morison, J., Lee, C., Rainville, L., Cole, S., Krishfield, R., Timmermans, M.-L., Toole, J., 2016. The beaufort gyre intensification and stabilization: A model-observation synthesis. J. Geophys. Res.: Oceans 121 (11), 7933–7952. http://dx.doi.org/10.1002/2016JC012196.